

## Comparison of simultaneous Na lidar and mesospheric nightglow temperature measurements and the effects of tides on the emission layer heights

Y. Zhao and M. J. Taylor

Center for Atmospheric and Space Sciences, Utah State University, Logan, Utah, USA

X. Chu

Department of Electrical and Computer Engineering, University of Illinois at Urbana-Champaign, Urbana, Illinois, USA

Received 9 June 2004; revised 25 September 2004; accepted 18 November 2004; published 18 February 2005.

[1] A detailed comparative study of two new mesospheric temperature data sets, measured by different remote-sensing techniques, has been performed as part of a long-term investigation of low-latitude mesospheric dynamics. Coincident observations using the University of Illinois Na wind/temperature lidar and the Utah State University CEDAR Mesospheric Temperature Mapper (MTM) were conducted from the summit of Haleakala Crater, Maui, Hawaii (20.8°N, 156.2°W, ~3000 m) as part of the Maui-MALT program. High-quality joint measurements were obtained during four lidar campaign periods, and 16 nights of data, spanning the interval January 2002 to October 2003, are presented here as example observations during each season. The Na lidar was coupled to the Air Force 3.7 m diameter steerable telescope providing exceptional quality temperature (and wind) data spanning the altitude range ~80–105 km. At the same time the MTM sequentially sampled the NIR OH (6,2) Meinel band and the O<sub>2</sub> (0,1) Atmospheric band nightglow emissions to determine the height-weighted mesospheric temperature at two nominal altitudes within this region. Comparison of these two nocturnal data sets shows exceptionally good agreement on a point-to-point, as well as a nightly mean basis, especially when allowances were made for physically reasonable changes in height during the course of the night for each of the nightglow layers. This analysis yields mean nocturnal altitudes of 88.6 km with a nocturnal variability of ±3.0 km for the OH M (6,2) band emission layer and 94.4 km for the O<sub>2</sub> (0,1) Atmospheric band mean altitude with a nocturnal variability of ±4.2 km. These results are in excellent accord with previous rocket, satellite and ground-based observations and further establish the validity of these two complementary measurement techniques. Furthermore, analysis of the computed height changes inferred from this study indicates a systematic decrease in altitude of both emission layers by up to several kilometers, whenever the lidar data showed evidence of strong diurnal or semidiurnal tidal forcing. The apparent downward trend in altitude was found to track the phase of the prevailing tidal motion providing new evidence for the effects of tides (or long-period gravity waves) on the height variability of the nightglow layers.

**Citation:** Zhao, Y., M. J. Taylor, and X. Chu (2005), Comparison of simultaneous Na lidar and mesospheric nightglow temperature measurements and the effects of tides on the emission layer heights, *J. Geophys. Res.*, 110, D09S07, doi:10.1029/2004JD005115.

### 1. Introduction

[2] Exploration of the Earth's mesosphere and lower thermosphere (MLT) region (~60–100 km) has revealed a wealth of structure and variability in the basic parameters: temperature, wind, pressure, and density. Of particular importance, for investigating the dynamics of the MLT region, are measurements of temperature. This is a funda-

mental parameter that provides direct information on the background structure of the atmosphere and on the ever-present effects of wave perturbations. A number of techniques have been developed to investigate mesospheric temperature and its variability. Most recently, these include resonant lidar soundings and satellite infrared limb-soundings, as currently performed by the SABER instrument on the TIMED satellite [e.g., *States and Gardner, 2000; Chu et al., 2001; Mertens et al., 2001*]. In particular, the development of sophisticated lidar techniques has provided an exceptional capability for probing the MLT region using

resonant scattering from metal atom layers such as sodium and potassium. Several powerful wind/temperature lidar systems now exist that are capable of determining temperature in the 80–105 km region at high precision ( $\sim 1\text{--}2$  K), with excellent temporal and vertical spatial resolutions. However, due to their complexity, they are usually operated on a limited or campaign basis [e.g., von Zahn *et al.*, 1987; She and Yu, 1994; Dao *et al.*, 1995; Gardner *et al.*, 1995; Zhao *et al.*, 2003; Chu *et al.*, 2005].

[3] This said, one of the longest and most established techniques for long-term measurements of mesospheric thermodynamics utilizes ground-based measurements of airglow emission rotational temperature. The most frequently used emissions are the near infrared OH Meinel bands and the O<sub>2</sub> (0,1) Atmospheric band. Relative intensity measurements of selected emission lines within these bands are employed to determine absolute rotational temperatures with high precision  $\sim 1\text{--}2$  K [e.g., Meriwether, 1984, 1989; Sivjee, 1992]. Careful selection of the emission features to satisfy local thermodynamic equilibrium [e.g., Pendleton *et al.*, 1993; Dodd *et al.*, 1994] provides a simple and robust technique for measuring atmospheric temperature integrated over the width of the emission layer. This technique is well developed and provides an important method for long-term monitoring of the nocturnal MLT environment [e.g., Bittner *et al.*, 2002; Burns *et al.*, 2002; Nielsen *et al.*, 2002].

[4] Early remote sensing measurements of the MLT region have shown that much of the observed variability is due to a broad spectrum of wave phenomena associated with atmospheric tides, planetary waves and gravity waves. The periodicities of these oscillations range from several minutes to hundreds of hours, while their horizontal scale sizes vary enormously from a few tens of kilometers to global scales. Atmospheric tides are a special case of global-scale oscillations occurring with periodicities that are fractions of a solar (or lunar) day [e.g., Chapman and Lindzen, 1970; Hagan *et al.*, 1995; Forbes, 1995]. The largest perturbations at MLT heights are usually associated with westward propagating diurnal (24-hour) and semidiurnal (12-hour) tides, generated by the absorption of solar radiation in various regions within the atmosphere. However, recent studies have also shown the importance of non-migrating tides in the MLT region [Talaat and Lieberman, 1999; Hagan and Forbes, 2002]. By their very nature, migrating tides are recurrent atmospheric features that display predictable characteristics (amplitudes and phases) for given seasons and latitudinal regions. Planetary waves are also global scale oscillations that exhibit periodicities of a few to several days, but their sources are more enigmatic. In contrast, gravity waves exhibit a range of periodicities (typically 5 min to several hours) and are episodic in nature, exhibiting significant day-to-day, seasonal, and geographic variability [e.g., Taylor and Hill, 1991; Swenson and Mende, 1994; Taylor *et al.*, 1995a, 1995b; Isler *et al.*, 1997; Wu and Killeen, 1996; Walterscheid *et al.*, 2001; Ejiri *et al.*, 2003; Nakamura *et al.*, 2003].

[5] Measurements of tides in the MLT region have been primarily made from satellites [e.g., Hays *et al.*, 1994; Burrage *et al.*, 1995; Shepherd *et al.*, 1995], from ground-based radars [e.g., Manson *et al.*, 1989, 2002; Franke and Thorsen, 1993; Hocking and Thayaparan, 1997;

Thayaparan, 1997; Singer *et al.*, 2003], and from Rayleigh and resonant lidars [e.g., Dao *et al.*, 1995; States and Gardner, 1998; She *et al.*, 2002], which have provided a wealth of data on the temporal and latitudinal structure of the migrating 12- and 24-hour solar tides. Remote sensing measurements of the naturally occurring nightglow emissions also provide an important tool for investigating upper atmospheric dynamics. Pioneering studies of the influences of tides on the MLT nightglow emissions were conducted by Fukuyama [1976] and Petitdidier and Teitelbaum [1977]. Subsequently, there had been several reports in the literature documenting ground-based observations of the diurnal, semidiurnal and the terdiurnal tidal signatures in the nightglow emissions [e.g., Takahashi *et al.*, 1984; Walterscheid *et al.*, 1986; Sivjee and Walterscheid, 1994; Wiens *et al.*, 1995; Reisin and Scheer, 1996; Hecht *et al.*, 1998; Pendleton *et al.*, 2000].

[6] One problem with the nightglow temperature measurements that makes them difficult to compare with observations by other instruments is the uncertainty in the altitude of the emission layer. Baker and Stair [1988] reviewed numerous rocket soundings from a range of sites that encompassed all seasons and established that the nocturnal OH emission layer originates at a nominal peak altitude of  $86.8 \pm 2.6$  km (half-power width  $8.6 \pm 3.1$  km). However, individual measurements used in this compendium study exhibited peak altitudes that spanned over 20 km in height from 77 to 99 km. More recently, satellite limb-soundings of the nightglow emissions have been used to investigate global variability in their altitude profiles which are in good agreement with the rocket measurements (within the expected uncertainties of the measurements). For example, Yee *et al.* [1997] used three days of data from the High Resolution Doppler Imager (HRDI) on the Upper Atmosphere Research Satellite (UARS), and determined a nominal peak altitude of  $89 \pm 4$  km for the OH emission. Likewise, most rocket and satellite investigations of the O<sub>2</sub> Atmospheric band emissions indicate a mean nocturnal peak altitude of  $94 \pm 2$  km [e.g., Witt *et al.*, 1979; Watanabe *et al.*, 1981; Murtagh *et al.*, 1990; Burrage *et al.*, 1994; Yee *et al.*, 1997]. This said, significant variability has been observed in the altitude of each of these emission layers as a function of latitude and local time, much of which has been attributed to the effects of atmospheric tides [e.g., Swenson *et al.*, 1989; Burrage *et al.*, 1994; Shepherd *et al.*, 1995; Yee *et al.*, 1997; Plagmann *et al.*, 1998; Fujii *et al.*, 2004]. However, information quantifying the local time altitude variability and its relationship to the predominant wave perturbations is still sparse for any given geographic location. This is due to the nature of satellite data which must be zonally averaged over a long period of time (yaw cycle), in order to successfully resolve the local time variability [e.g., Hays *et al.*, 1994; Roble and Shepherd, 1997].

[7] The Maui-MALT program is a joint research initiative between the U.S. Air Force Office of Scientific Research (AFOSR) and the National Science Foundation (NSF). Measurements are obtained using a cluster of instruments operated at the Air Force AEOS facility at the summit of Haleakala Crater, Maui (20.8°N, 156.2°W). These instruments include a powerful Na wind/temperature lidar (operated on a campaign basis), a meteor radar, and several passive imaging instruments designed for long-term unat-

tended measurements of the MLT nightglow emissions. One of the goals of this program is the investigation of the thermal structure and variability in the MLT at low-latitudes. Previous measurements during the ALOHA-93 campaign have revealed a wealth of gravity wave activity over the central Pacific ocean [e.g., *Hecht et al.*, 1995; *Swenson et al.*, 1995; *Taylor et al.*, 1995a, 1995b, 1995c], and much larger than expected tidal amplitudes (typically  $>20$  K at 90 km) [*Dao et al.*, 1995; *Hecht et al.*, 1995, 1998]. In contrast, the global scale wave model (GSWM), which computes the response of the atmosphere to thermally driven diurnal and semidiurnal tides over a broad altitude range [*Hagan et al.*, 1999], indicates that the diurnal tide should dominate the MLT region over Hawaii ( $21^\circ\text{N}$ ), but with a typical amplitude of  $\sim 6\text{--}6.5$  K at 90–95 km during the fall, winter and spring months. Moreover, the semidiurnal tide is expected to be of smaller amplitude at  $\sim 3\text{--}5$  K during these months. These predicted temperature perturbations are clearly much smaller than those measured during the ALOHA-93 campaign during the fall equinox period. During the summer months, both the diurnal and semidiurnal tidal components are expected to be quite small at 2–3 K.

[8] In this paper, we utilize coincident temperature measurements collected by the University of Illinois (UIUC) Na wind/temperature lidar (operated on a campaign basis), and the Utah State University (USU) CEDAR Mesospheric Temperature Mapper (MTM). The measurements were made as part of the Maui-MALT program, to investigate altitude variability in the nocturnal NIR OH (6,2) and O<sub>2</sub> (0,1) emission layers and to study the effects of strong tides on the layer heights. First, a detailed comparison of these two independent data sets was performed to establish the limits of their compatibility, which is important for seasonal investigations of the MLT dynamics (over 400 nights of MTM data have been obtained to date). The results of this comparison are then utilized to study the nocturnal mean altitude of each emission layer, its local time variation, and the apparent association with the prevailing tidal/gravity wave forcing at low-latitudes. Our height results agree very well with an ensemble of previous rocket, satellite and ground-based measurements that have proven to be so consistent over the past 30 years. However, our analyses also show significant systematic variability in height (centered about the well-defined mean) that appears to be related to the phase of strong prevailing tidal motions.

## 2. Instrumentation and Observations

### 2.1. Mesospheric Temperature Mapper

[9] The CEDAR Mesospheric Temperature Mapper (MTM) is a high performance imaging system capable of precision measurements of the intensity and rotational temperatures, of the near infrared OH and O<sub>2</sub> nightglow emission layers which, as discussed earlier, occur at nominal peak altitudes of  $\sim 87$  and  $\sim 94$  km respectively. Briefly, the MTM utilizes a high quantum efficiency CCD array coupled to a wide-angle telecentric lens system ( $90^\circ$  field of view centered on the zenith) to observe selected emission lines in the OH (6,2) Meinel band and the O<sub>2</sub> (0,1) Atmospheric band. Sequential measurements were made using a set of narrow band ( $\Delta\lambda \sim 1.2$  nm) filters centered on the OH P<sub>1</sub>(2) and P<sub>1</sub>(4) lines at 840 and 846.5 nm and

two well-defined regions of the O<sub>2</sub> (0,1) Atmospheric band at 866 and 868 nm. Each emission was observed for 60 sec followed by a background sky measurement at 857 nm, resulting in a cycle time of  $\sim 5.5$  min. The data were spatially summed on the CCD to form a  $128 \times 128$  super pixel image with a resultant zenithal pixel footprint of  $\sim 0.9 \times 0.9$  km at 90 km altitude.

[10] Rotational temperatures were computed separately for the OH and the O<sub>2</sub> emissions using the well-established “ratio method”, as described by *Meriwether* [1984]. For the OH measurements, a value of 1.300 was used for the ratio of the transition probabilities  $A[P_1(4)]/A[P_1(2)]$ . This value was determined from the recently updated line parameters by *Goldman et al.* [1998]. Based on typical OH and O<sub>2</sub> emission levels measured at Maui, the precisions of the measurements were determined to be  $<0.5\%$  (in 1 min) for the individual line emission intensities, and  $<1\text{--}2$  K (in 3 min) for the derived OH and O<sub>2</sub> rotational temperatures. A previous comparison of the MTM OH rotational temperatures with other well calibrated instruments (an FTIR spectrometer and the Colorado State University Na temperature lidar) has shown that our nightly mean temperatures, referenced to the 87 km lidar temperatures, are accurate to about  $\pm 5$  K [*Pendleton et al.*, 2000]. The O<sub>2</sub> measurements described herein are a recent addition in capability of the MTM that was implemented as part of the Maui-MALT program. Cross-calibration using coincident spectrometric data has yet to be performed but measurements alongside the UIUC Na lidar, obtained as part of this program, show a similar magnitude for the uncertainty of the O<sub>2</sub> nightly mean temperatures (estimated at  $\pm 6$  K), as referenced to the 94 km lidar temperatures. Further details of the MTM data reduction and analysis method are given in *Pendleton et al.* [2000] and *Taylor et al.* [1999, 2001].

[11] The MTM was installed in an Optics Trailer located on the roof of the AEOS facility, Maui, HI, in November 2001. The camera operates automatically from dusk to dawn (for solar depression angles  $>12^\circ$ ) for typically 23 nights each month (centered on the new moon period). Data are stored locally on computer disk and are downloaded at regular intervals via the internet to USU for subsequent analysis. To date, over 400 nights of quality data (of duration  $>4$  hours per night) have been obtained, providing detailed information on the nocturnal and seasonal behavior of mesospheric temperature and its variability at these two emission heights.

### 2.2. Na Wind/Temperature Lidar

[12] The UIUC Na wind/temperature lidar utilized for the Maui-MALT program is a large-aperture steerable narrow-band resonance fluorescence lidar capable of high precision temperature and wind measurements over the Na layer (centered at  $\sim 90$  km altitude). The lidar was installed at the AEOS Facility at the summit of Haleakala, Maui, HI, and coupled with the AEOS large aperture (3.67 m) astronomical telescope. The steering ability was achieved by transmitting the lidar beam through the primary mirror of the telescope, resulting in a  $\sim 40$  m diameter footprint at the Na layer altitude range. Backscattered photons were then collected by the primary mirror, and returned through the same optical path to the lidar receiver. The lidar was operated at a repetition rate of 50 Hz using laser pulses

**Table 1.** Summary of the Lidar and MTM Observation for the 16 Nights of Coincident Data

UT Date	Na Lidar		MTM		Coincident Time, hours
	Start Time	End Time	Start Time	End Time	
9 Jan. 2002	6.8	15.2	6.8	13.7	6.8
14 Jan. 2002	5.5	11.1	5.0	16.1	5.6
15 Jan. 2002	5.0	16.0	5.0	16.1	10.9
9 April 2002	5.1	15.9	8.4	15.2	6.7
11 April 2002	6.7	15.8	5.7	14.9	8.2
7 July 2002	7.2	15.4	6.0	15.3	8.1
9 July 2002	7.3	15.4	6.0	14.9	7.6
13 July 2002	10.2	15.2	6.0	14.9	4.7
14 July 2002	5.8	15.3	6.0	14.9	9.2
15 July 2002	6.4	15.3	6.0	14.9	8.5
21 Oct. 2003	8.4	15.9	5.8	13.7	5.5
23 Oct. 2003	7.7	15.5	5.8	15.5	7.8
24 Oct. 2003	9.5	15.9	5.8	15.5	6.0
26 Oct. 2003	4.4	15.9	5.8	15.5	9.5
28 Oct. 2003	5.3	15.9	5.8	15.5	9.5
30 Oct. 2003	5.2	11.6	5.8	15.5	5.8

with a spectral width of 60 MHz (RMS) and an energy of 20–35 mJ per pulse.

[13] A three-frequency technique was used to simultaneously measure temperature, radial wind, and Na density [She and Yu, 1994; States and Gardner, 2000]. Briefly, a continuous wave ring dye laser was locked to a Doppler-free hyperfine feature near the Na  $D_{2a}$  line peak (589.158 nm), using a Na vapor cell to provide the peak frequency  $f_0$ . A dual-acousto-optic modulator was then used to shift the laser frequency by  $\pm 630$  MHz to generate two wing frequencies  $f_{\pm}$ . To eliminate the effects of Na density fluctuations on the temperature and wind measurements, the lidar frequency was switched from  $f_0$  to  $f_+$  and then to  $f_-$  every second (i.e., after 50 laser-pulses). A total of 1500 laser pulses were summed at each frequency resulting in an integration time of 90 s for one complete 3-frequency measurement. A more detailed description of the Maui-MALT Na lidar system can be found in an accompanying paper by Chu *et al.* [2005].

[14] Two operating modes are employed at Maui to obtain the wind and temperature measurements. One aims the lidar beam at the zenith (Z) and then  $30^\circ$  off zenith to the north (N), east (E), south (S), and west (W) using the sequence ZNEZSW. As it takes  $\sim 30$  s to steer the telescope to each position, a complete sequence of measurements is obtained every  $\sim 12$  minutes. This is the primary mode of operation providing detailed measurements of the horizontal wind and temperature field over the  $\sim 80$ – $105$  km range. The second mode simply points the lidar beam at the zenith direction throughout the night for high-resolution temperature measurements. This mode has a much higher sample rate ( $\sim 90$  s) and was designed to investigate short-period gravity waves, it is also best suited for coordinated studies with the MTM data set. However, for this comparative study, data from both operational modes are used.

[15] On firing a laser pulse, the lidar triggers a multi-channel scaler to start to count the flight time from the moment that the laser pulse is transmitted, to the moment that the backscattered photons are detected by the receiver. The altitude of the scattered photons can be determined from the flight time. The returned photons are recorded as range-resolved photon count profiles integrated for 90 s. As the laser pulse duration is only 5–7 ns, the raw photon data

were collected at a high vertical range resolution of 24 m, and then binned to 480 m resolution to derive temperature, radial wind, and Na density from the ratio of the photon counts at three different frequencies as described in States and Gardner [2000]. The processed data were then spatially and temporally smoothed using a 2-D Hamming window with full widths of 1-km and 0.5-hour. The data are set to a uniform grid with 100-m vertical resolution and 15-min temporal resolution. A detailed error analysis of the Na wind/temperature lidar has been given by Papen *et al.* [1995]. The measurement error is dominated by the photon noise errors, which were computed following the method given in States and Gardner [2000]. A major advantage of the large AEOS telescope aperture at Maui is the high returned photon signal levels which result in an uncertainty of  $< 1$  K in the temperature measurements at the peak of the Na layer, for a 90-sec integration and 480-m spatial resolution. The absolute temperature error of the smoothed data used for this study is typically 1–2 K over the altitude range  $\sim 85$  to 105 km.

### 3. Analysis and Results

[16] Since January 2002, there have been five successful campaign periods where detailed coincident measurements of the mesospheric temperature field have been obtained by the Na lidar and MTM system together with other associated measurements. For this initial comparative study, four campaign periods comprising 16 nights of joint data are used sampling each of the seasons: three nights in January, two in April, and five in July, 2002, followed by six nights in October 2003. On each of these occasions, coincident data were obtained for extended periods of time (ranging from  $\sim 4.5$  to  $\sim 11.0$  hours in duration) and totaling over 120 hours of high-quality measurements. A summary of the lidar and MTM observations for each of these nights is given in Table 1. The average nocturnal duration of the joint measurements was  $\sim 7.5$  hours.

#### 3.1. MTM and Na Lidar Data

[17] Figure 1 compares the MTM and Na lidar temperature data recorded on the 11 April 2002 (UT day 101). Figure 1a shows the MTM temperature data OH (open

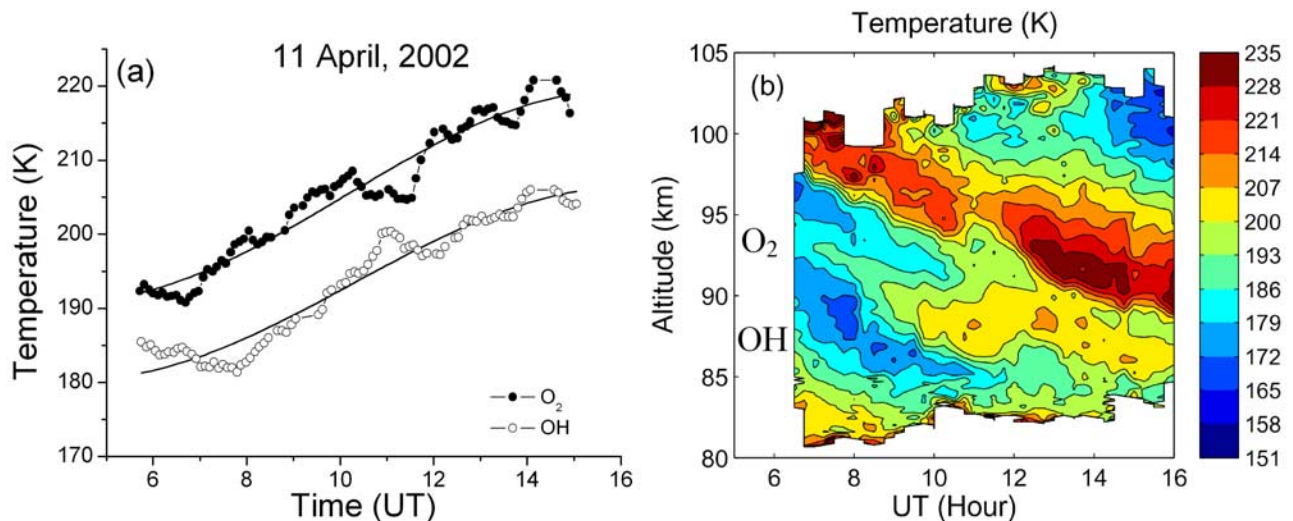


**Figure 1.** Example of coincident MTM and Na lidar temperature data for 11 April 2002. (a) Five-point smoothed OH (open circles) and O<sub>2</sub> (solid circles) temperatures (the solid lines show a forced 24-hour fit to each data set). (b) Lidar temperature contours versus UT time for the same period. The nominal peak heights of the OH and O<sub>2</sub> data are indicated.

circles) and O<sub>2</sub> (solid circles) for this night. The data have been averaged over a  $5 \times 5$  superpixel region ( $4.5 \times 4.5$  km) centered on the zenith, for more direct comparison with the lidar measurements. On this night, continuous observations ( $\sim 5.5$  min/sample) were obtained over an  $\sim 9$ -hour period (from 6–15 UT) and comprised 86 temperature measurements at each emission altitude characterized by a precision of about  $\pm 2$  K. To highlight the main features of the data, both plots have also been 5-point smoothed. The same characteristic shape and slowly increasing temperature with time are evident in both plots but they are separated in magnitude by  $\sim 10$  K (with the O<sub>2</sub> temperatures consistently hotter). The observed increase in temperature during the course of the night was  $\sim 25$  K for both data sets. The smaller-scale variations superimposed on the gradual trend are also quasi-coherent and are most probably due to short-period ( $\sim 1$ – $5$  hours) gravity waves. The quality and form of these data are typical of many of the nocturnal measurements obtained by the MTM at Maui, especially around the equinox period.

[18] Figure 1b shows a contour plot of the processed Na lidar temperature data obtained on this night for the altitude range  $\sim 80$ – $105$  km. As noted earlier, the data have been smoothed using a 1-km wide, 0.5-hour (full-width) Hamming window resulting in an effective vertical resolution of 0.1 km and a temporal resolution of 15 min. For this comparison, all of the available lidar data were utilized (i.e., data from each pointing direction (Z, N, S, E, W) were treated the same). This assumes that the off-zenith temperature profiles within  $\pm 30^\circ$  (corresponding to a mesospheric footprint of  $\sim 50$  km radius) are essentially homogeneous and are valid for the long-period perturbations that are of particular interest herein. The data are visually dominated by a large-scale, coherent oscillation that exhibits a marked downward phase progression of  $\sim 1$  km/h, and vertical wavelength of  $\sim 24$  km, characteristic of the diurnal tide [e.g., Forbes, 1995]. The measured amplitude was unusually large at  $\sim 20$  K at 94 km. Previous tidal studies from

this site during the ALOHA-93 campaign have also reported similar magnitude diurnal tidal amplitudes during the fall equinox period [e.g., Dao *et al.*, 1995; Hecht *et al.*, 1995]. A concurrent tidal signature was also evident in the lidar meridional and zonal wind data with a similar vertical wavelength and phase speed (data not shown).

[19] Comparison of the lidar data with the MTM data of Figure 1a immediately clarifies the origin of the near uniform increase in temperature with time that was observed for both nightglow emissions on this occasion. For example, at the 94 km level (typical O<sub>2</sub> peak altitude) the lidar contour plot shows an initial temperature of  $\sim 190$  K that gradually increases with time as the phase of the diurnal tides progresses downwards. The highest O<sub>2</sub> temperatures occurred around 14:00 UT near the end of the night when the tidal perturbation temperature was largest. A similar situation arises for the OH temperature data, but due to its lower nominal peak altitude ( $\sim 87$  km), the measurements reflect a predominantly cooler portion of the tidal wave field. To emphasize the consistency of these two independent data sets, the solid curves superimposed on the MTM data, show a forced diurnal (24-hour) tidal fitting to the MTM data showing very good qualitative agreement. (Note the data are of insufficient length to determine the periodicity). Furthermore, the fitted data yield similar wave amplitudes  $\sim 13$  K (OH) and  $\sim 14$  K (O<sub>2</sub>), which compare reasonably well with fitted amplitudes of 15 K (87 km) and 20 K (94 km) from the lidar data. A more detailed comparison of the lidar and MTM data is given later in this section (see Figures 4 and 5). Here it is important to note that the MTM and lidar data sets both exhibit the same temperature values and nocturnal trends (within the uncertainty of the instrumental measurements), in response to the large dynamical perturbation, indicating high qualitative agreement.

[20] Figure 2 shows coincident OH and O<sub>2</sub> data for three further selected nights representative of the winter, summer and late fall period MTM data sets. All three are plotted on the same temperature and time scales to permit direct

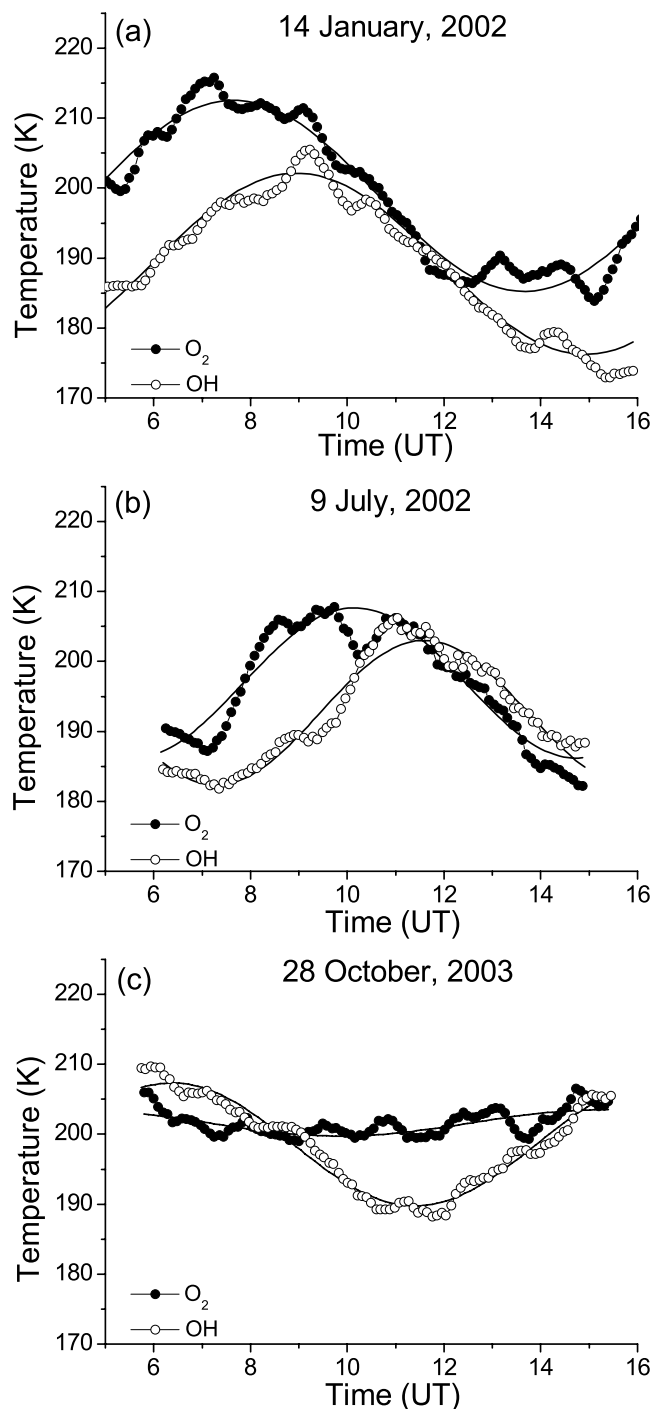


**Figure 2.** MTM data for three additional example nights selected from the winter, summer, and late-fall seasons. The figure format is the same as Figure 1a, and in each case the solid lines show the least squares fit to the smoothed data. (a) A well-defined  $\sim 12$ -hour oscillation, (b) an  $\sim 8$ -hour perturbation, and (c) an  $\sim 10$ -hour wave motion.

comparisons. Figure 2a shows a well-defined, long-period oscillation observed on 14 January 2002 (UT day 14). The same oscillation is evident in both temperature data sets with a distinct phase shift, with the  $O_2$  temperature perturbation leading the OH temperature data. The mean temperature of the OH and  $O_2$  data sets are separated

by  $\sim 10$  K and both exhibit superimposed smaller-scale gravity waves, in this case exhibiting periodicities of  $\sim 1$ – $2$  hours. To investigate the properties of the long-period perturbation, the solid curves show a sinusoidal fit of the form  $A \sin(2\pi t/\tau + \phi)$  to the raw OH and  $O_2$  temperature data sets (where  $A$  is the amplitude,  $\tau$  is the observed wave period and  $\phi$  is the phase). The fitted periodicity of the wave observed in both the OH and the  $O_2$  data was  $12.0 \pm 0.2$  hours. Both plots also exhibited similar amplitudes of  $13.0 \pm 0.4$  K and a distinct phase shift of  $1.3 \pm 0.3$  hours. These results are quite consistent with downward phase progression associated with the semidiurnal tide [e.g., *Forbes, 1995*]. The derived OH and  $O_2$  band intensity data (not shown) also exhibited clear  $\sim 12$ -hour tide-like signatures. However, due to the limited nocturnal duration of our lidar and MTM data sets, an unequivocal determination of the tidal modes is impossible.

[21] The remaining plots in Figure 2 show summer time data for 9 July 2002 and late fall data for 28 October 2003. The July data are characterized by a shorter period oscillation with a least squares fit of  $9.2 \pm 0.3$  hours and  $8.6 \pm 0.2$  hours for the  $O_2$  and OH temperature data respectively, amplitudes of  $10.7 \pm 0.6$  K ( $O_2$ ) and  $10.3 \pm 0.4$  K (OH), and a phase shift of  $1.6 \pm 0.2$  hours ( $O_2$  leading OH). Our MTM data for the July and August 2002 time interval were often characterized by quasi-8-hour period oscillations possibly indicating the presence of a strong terdiurnal tidal component at this time. A detailed investigation of the MTM temperature signatures during this period, together with coincident meteor wind radar measurements, is given by *Taori et al. [2005]*. In comparison, the data for the 28 October (Figure 2c) show significant differences in the apparent shape and amplitude of the long-period perturbation evident in both the OH and  $O_2$  temperature data sets. The OH temperature data exhibited the largest variation during the night with a deep minima around 11–12 UT, whereas the  $O_2$  temperature data show only a shallow minima around 10 UT. A least squares analysis of these two data sets yields a similar periodicity of  $\sim 10$ – $11$  hours and amplitudes of 8.8 K (OH) and 1.9 K ( $O_2$ ). Both data sets again exhibit significant coherent short-period gravity wave activity. Together these four examples illustrate considerable seasonal variability in the nocturnal mesospheric temperatures observed from this low-latitude site. In each case, the primary variations were wave-like in nature and were most probably the result of different tidal (or long period gravity wave) forcing during the different seasons [e.g., *Manson et al., 1989, 2002; Burrage et al., 1995; States and Gardner, 2000; Hagan and Forbes, 2002*].

[22] Figure 3 shows the 2-D color contour plots for the lidar temperature data obtained on each of the four nights discussed in Figures 1 and 2. For various reasons the duration of the lidar data is different for each of these nights, but to facilitate the data comparison, all are plotted on the same timescale as the MTM data. Each lidar plot is characterized by a different long-period wave feature, but all show marked downward phase progression normally associated with tidal or long-period gravity wave activity. For example, the apparent downward phase progression ( $\sim 1$  km/h) and short vertical wavelength ( $\sim 24$  km) of the perturbation observed in the lidar data of 11 April and discussed in Figure 1b is most consistent with a diurnal tidal

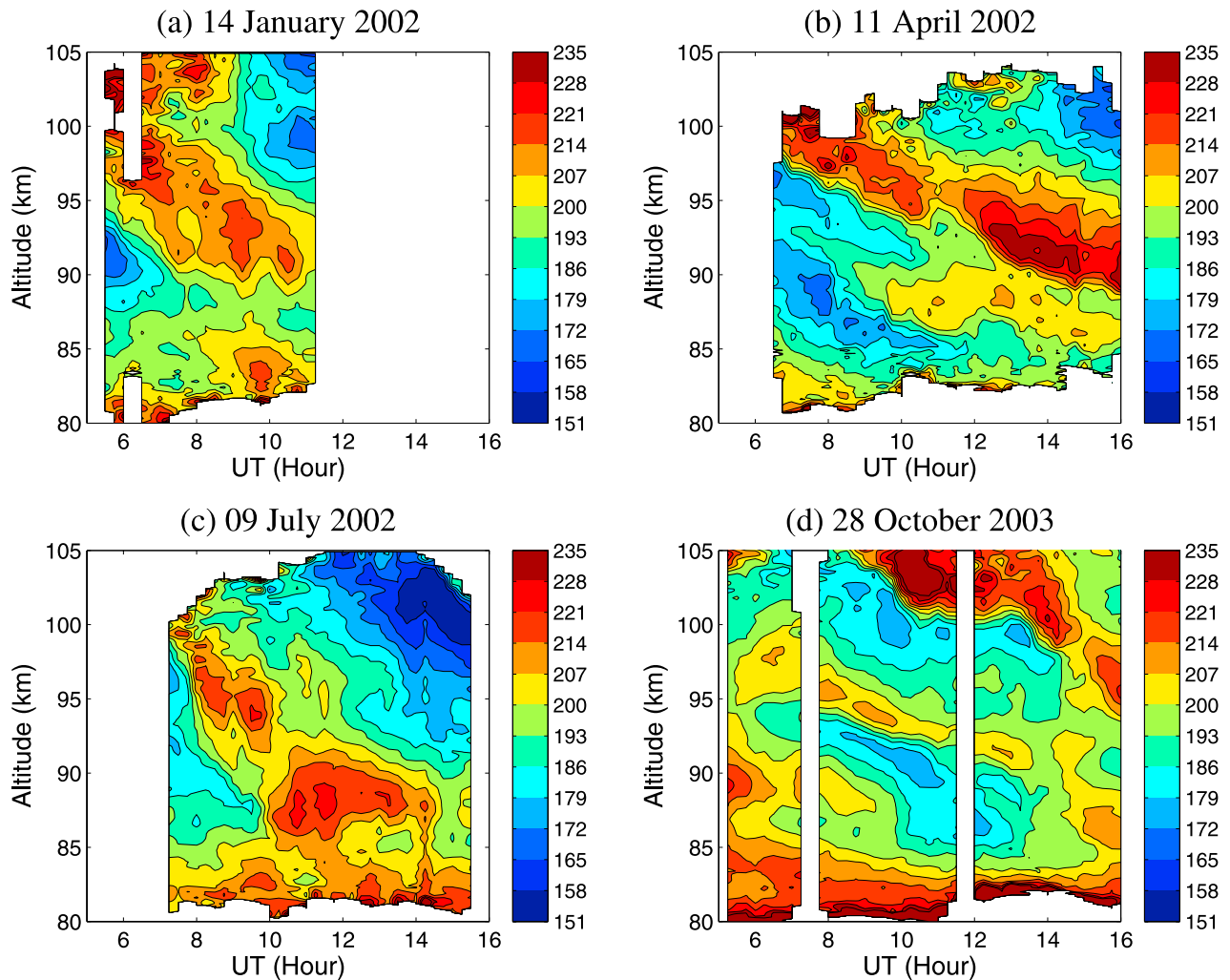


**Figure 3.** Color contour plots showing the lidar temperature data for the four example nights. The altitude and timescales are the same for each plot to highlight the difference in the phase speeds of the dominant tidal/long-period gravity waves.

signature. (For comparison these data are reproduced here as Figure 3b.) In contrast, the tidal signature evident on 14 January (in Figure 3a) was significantly steeper and exhibited a larger vertical wavelength. Due to the finite altitude range of the lidar data, it is not possible to measure directly the vertical wavelength of this perturbation. However, estimates of the downward phase progression for this night ( $\sim 3\text{--}4$  km/h) are consistent with a semidiurnal tidal perturbation with an inferred vertical wavelength of about 36–48 km. This interpretation is in good agreement with the MTM temperature measurements (Figure 2a) which were obtained for a significantly longer period of time than the lidar data and show a large amplitude  $\sim 12$ -hour oscillation. In comparison, our coincident summertime MTM and lidar data show less well-formed tidal structures that were not as coherent over the full altitude range sampled by the lidar, possibly due to the presence of other significant perturbations. For example, the lidar data of 9 July (Figure 3c) was dominated by a long-period oscillation with a downward phase progression but the data also contains clear evidence of overturning in the 85–90 km level temperature structure around 12 UT. Finally, the long-

period perturbation recorded on 28 October (Figure 3d) exhibited a well-defined phase slope of  $\sim 1$  km/h, similar to that expected for the diurnal tide (e.g., Figure 3b); however, in this case the estimated vertical wavelength from the lidar data was much shorter ( $\sim 10$  km), suggesting it was probably not tidal in origin.

### 3.2. Fixed Altitude Temperature Comparison

[23] As the Na lidar and MTM temperature determinations are based on two separate measurement techniques, resulting in different altitudinal and temporal resolutions, it was necessary to weight the data in order to make meaningful comparisons. The Na lidar utilizes a 3-frequency measurement technique to determine atmospheric temperature over a large number of sampled altitudes within the range  $\sim 80\text{--}105$  km. In contrast, the MTM temperature data depend on observations of selected emission lines, which are naturally height-weighted over the finite thickness of the airglow layer profiles (typically 8–10 km full-width at half-maximum, FWHM) to determine the OH and O<sub>2</sub> rotational temperatures. As already mentioned, the two emission bands used herein are well-studied in the literature and

have been shown to be in local thermodynamic equilibrium, thereby providing a reliable measure of atmospheric temperature weighted over the height of the respective airglow emission layers.

[24] A number of studies in the literature have tackled this problem [e.g., *Takahashi et al.*, 1998; *Melo et al.*, 2001; *Fujii et al.*, 2004]. In particular, previous studies using joint lidar and airglow data range from basic comparisons using the lidar data at a single (fixed) height, coinciding with the expected peak altitude of the emission layer, to sophisticated treatments which utilize the lidar temperatures to reproduce a Gaussian-weighted intensity distribution for the specific emission lines used in the airglow temperature determinations [e.g., *She and Lowe*, 1998; *von Zahn et al.*, 1987]. This latter technique has been applied to OH data only. Here we wish to compare temperatures derived from both the OH and the O<sub>2</sub> emission layers. For this initial study, we have convolved each 15-min lidar temperature profile with a Gaussian profile to approximate the brightness-weighted temperatures as a function of time, for both the OH and O<sub>2</sub> emission data as measured by the MTM. As pointed out by *She and Lowe* [1998], this technique will suffer from a small error due to the nonlinear variation of intensity with temperature. However, for the limited nocturnal and seasonal range in mesospheric temperatures evident at low-latitudes, the effect is expected to be very small (<1 K), except in the presence of steep temperature gradients (~10 K/km) where an uncertainty of a few K can occur. Our approach is therefore a compromise, but should be quite satisfactory for the current investigation given the expected uncertainties in the two data sets.

[25] In the following analyses, we have height-weighted the lidar temperature data (available with an interpolated 0.1-km vertical resolution) using a Gaussian function with a FWHM of 9.3 km ( $1/e \sim 5.6$  km). This weighting function was selected based on the results of the HRDI measurements from the UARS satellite which agree well with previous rocket sounding of these two airglow layers [e.g., *Watanabe et al.*, 1981; *Baker and Stair*, 1988; *Takahashi et al.*, 1996; *Yee et al.*, 1997]. The weighting was centered at 87 and 94 km respectively which, as mentioned earlier, are commonly accepted in the literature as the nominal nocturnal peak altitudes for the OH and the O<sub>2</sub> emission layers. The MTM temperature data were binned to 15 min time interval for direct comparison with the lidar data.

[26] Figure 4 compares the lidar data weighted in this manner with the MTM data for two of our four example nights. To aid a visual comparison, each of the figures is plotted with the same temperature and timescales. Figure 4a shows the results of this comparison for the OH temperature data of the 11 April. The figure is divided into two parts: the upper plot shows the temperature versus time for the MTM (solid circles) and the Gaussian-weighted lidar data (open circles). The lower plot illustrates the quality of the comparison as a function of time, using the magnitude of the difference between the individual (15-min) MTM and lidar data samples. On this night, the individual deviations were small (all < 4 K) with a Root-Mean-Square (rms) difference of 2.3 K. This result is clearly reflected in the high degree of correlation evident between the two data sets plotted in the upper panel. Figure 4b shows the corresponding results for

the height-weighted lidar and the O<sub>2</sub> MTM temperature data. In this case, the data are separated by several K, with the MTM data being consistently hotter. This difference is quantified by a significantly higher rms value of 6.7 K. Thus, on this occasion, the lidar and the OH temperatures agree very well, whereas the lidar comparison with the O<sub>2</sub> temperature data show the same general trends and smaller-scale features but a substantial offset in their absolute temperatures throughout the night.

[27] In contrast, the data for 9 July (Figures 4c and 4d) show the opposite situation where the height-weighted lidar and the O<sub>2</sub> temperature data (Figure 4d) now indicate very good agreement throughout the night (as indicated by the low rms difference of 2.8 K), whereas the OH and lidar temperature measurements exhibit like-temporal variability, but a significant 9.9 K rms mean separation (with the MTM data consistently colder). These two data sets were selected to highlight the variability in the agreement resulting from this comparison study and, equally importantly, to show that the differences observed from night-to-night, and during the course of the year were not apparently systematic in nature, indicating that they were most probably due to geophysical processes possibly associated with altitude changes in the emission layers.

[28] A summary of the 16 nights of comparative measurements is given in Table 2. For each emission, the mean nightly rms difference is indicated for fixed peak altitudes of 87 and 94 km for the OH and O<sub>2</sub> temperature data respectively. Examination of this table shows that for the OH comparison, the nightly mean temperature differences (MTM-lidar) ranged from about +3 to -12 K, which results in an rms value of 6.0 K for the full data set. The results for the O<sub>2</sub> temperature comparison indicated mean nocturnal temperature differences ranging from -3 to +11 K, with a nocturnal average rms difference of 6.6 K. In summary, assuming nominal peak altitudes for the two airglow emissions for all four seasons, the rms difference between the nightly averaged OH and O<sub>2</sub> MTM temperatures and the Gaussian-weighted lidar data were similar at ~6-7 K.

### 3.3. Variable Altitude Temperature Comparison

[29] In the preceding analysis, the level of agreement between the lidar and MTM data sets varied substantially from night-to-night and during the course of the night, suggesting that further improvements in the comparison are possible. This is to be expected as a number of previous theoretical and observational studies have shown considerable variability in the altitude of the emission layers possibly due to tides and gravity waves [e.g., *Swenson et al.*, 1989; *Burrage et al.*, 1994; *Shepherd et al.*, 1995, 1998; *Roble and Shepherd*, 1997; *Swenson and Gardner*, 1998; *Ward*, 1998; *Hickey et al.*, 2000; *Liu and Swenson*, 2003].

[30] To investigate this possibility, we have reanalyzed the lidar data with a variable peak altitude for each airglow data set. For example, for the lidar/O<sub>2</sub> comparison, the lidar data were height-weighted using the same format Gaussian function, but values were computed for an assumed peak altitude that varies over  $\pm 6$  km in height (in 0.1 km steps), centered on the nominal peak at 94 km. This range lies well within the altitude range sampled by the lidar providing high confidence in this approach. The best fit height was then determined by minimizing the difference between the

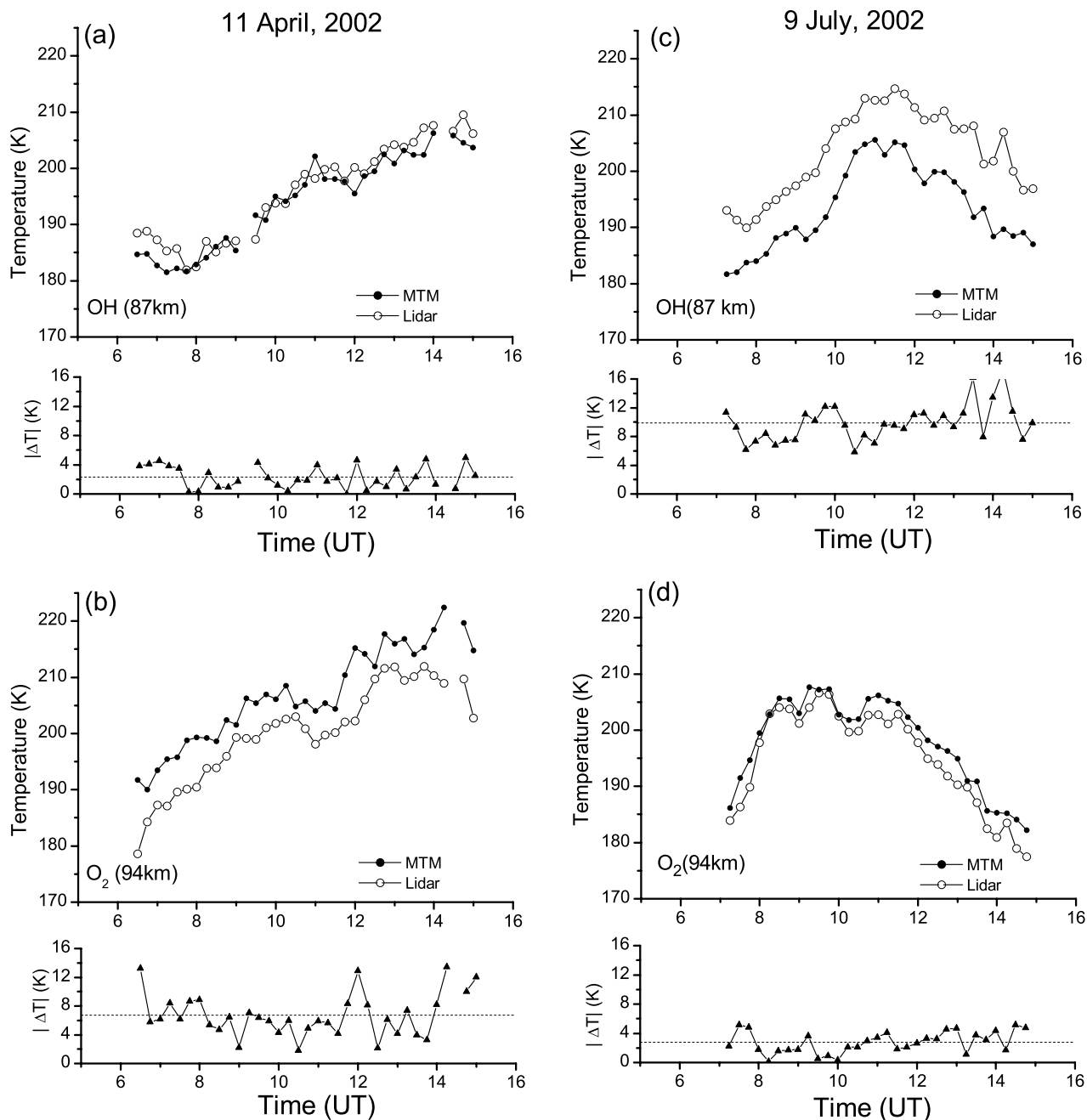


**Figure 4.** Comparison of the Gaussian-weighted lidar temperature data (open circles) with MTM (solid circles) for fixed peak altitudes of 87 km (OH) and 94 km (O<sub>2</sub>). Two example nights are shown; (a and b) 11 April and (c and d) 9 July. The lower panel in each plot indicates the difference between the two data sets as a function of time. The dashed lines indicate the nightly rms deviation.

two data sets for each 15-min data sample. Figure 5 shows the results of this study applied to the O<sub>2</sub> data for each of the four example nights. It is immediately evident that by changing the peak altitude of the lidar weighting function many of the differences that arose between the two data sets, when assuming a fixed O<sub>2</sub> emission altitude, can be fully accounted for. This is particularly evident in Figure 5c which now shows essentially total agreement throughout the ~8 hours of coincident measurements obtained on 9 July. This result is quantified by the large reduction in the rms deviation down from 2.8 K (for the fixed altitude study) to

0.8 K. (Note some minor differences did still arise for a short interval around ~9 UT.) A similar level of agreement was achieved for the data of 14 January and 28 October (Figures 5a and 5d) where, for short periods of time, minor discrepancies of <2K arose. In contrast, the data of 11 April (Figure 5b) show a different behavior with excellent agreement for the first 3 hours of coincident observations, but thereafter significant differences occurred for the rest of the night (with similar magnitudes to those obtained during the fixed altitude study). The computed altitudes needed to achieve the improved agreement in these four example data

**Table 2.** Summary of 16 Nights of Comparative Lidar and MTM Temperature Data Indicating the Nocturnal Mean Temperatures for Fixed Nominal Altitudes of 87/89 (OH) and 94 (O<sub>2</sub>) and for Variable Emission Altitudes Together With Their Inferred Nightly Mean Peak Altitudes<sup>a</sup>

Date	O <sub>2</sub>					OH					
	MTM	Na Lidar (94)	rms ΔT (94)	rms ΔT (Z <sub>0</sub> )	Peak Altitude	MTM	Na Lidar (87)	rms ΔT (87)	rms ΔT (89)	rms ΔT (Z <sub>0</sub> )	Peak Altitude
9 Jan. 2002	185.9	182.7	3.9	0.6	95.0	193.3	204.6	11.3	5.4	0.8	90.5
14 Jan. 2002	207.2	201.1	6.1	2.1	94.2	196.2	198.6	2.7	3.1	1.1	88.9
15 Jan. 2002	196.0	196.3	3.9	1.6	93.4	196.9	208.1	11.2	6.5	2.1	91.9
9 April 2002	216.4	207.2	9.3	7.0	93.7	207.2	203.9	3.8	2.3	0.8	87.9
11 April 2002	206.8	200.1	6.7	3.5	94.4	194.2	195.7	2.3	3.0	0.8	86.7
7 July 2002	192.5	190.2	3.9	2.1	93.0	181.8	189.0	7.8	8.2	5.2	88.3
9 July 2002	197.8	195.1	2.8	0.8	93.6	193.6	203.4	9.9	7.7	3.1	90.9
13 July 2002	196.5	185.7	10.8	4.6	95.6	183.4	190.7	7.3	5.2	2.3	91.5
14 July 2002	191.0	193.7	3.6	0.8	93.8	181.4	193.2	11.9	10.9	6.8	88.9
15 July 2002	196.8	191.9	4.9	2.1	94.9	183.0	185.3	2.8	3.9	2.1	85.6
21 Oct. 2003	212.3	206.1	6.3	4.8	94.5	194.3	199.8	5.8	4.4	4.3	89.1
23 Oct. 2003	198.7	192.6	6.2	0.8	94.1	198.7	201.2	2.9	2.0	0.5	88.2
24 Oct. 2003	213.6	203.4	10.2	1.3	92.7	217.3	216.9	2.4	3.8	0.9	85.6
26 Oct. 2003	206.9	197.4	9.7	2.6	96.5	204.4	203.2	3.8	3.8	1.6	86.6
28 Oct. 2003	201.8	195.0	6.8	1.7	96.3	198.9	199.4	1.6	2.4	0.4	87.6
30 Oct. 2003	199.3	189.5	10.1	1.8	97.7	192.3	201.0	8.7	3.0	1.3	90.2
Average	201.2	195.5	6.6	2.4	94.6	194.8	199.6	6.0	4.7	2.1	88.7

<sup>a</sup>For each method the rms differences are given for both emissions.

sets ranged from  $\sim 92$ – $98$  km. A detailed discussion on the nature of these height changes is given in section 4.

[31] A similar reanalysis procedure was performed on the lidar/OH temperature comparison. However, due to the lower peak altitude of the OH emission ( $\sim 87$  km), it was sometimes necessary to truncate the Gaussian-weighting profile when it was well below the nominal OH peak altitude. This situation depended on the magnitude of the uncertainties in the lidar temperature data which tended to increase near the base of the Na layer where the signal was lowest. This said, the dominant signals contributing to the height-weighting reside close to the Gaussian peak and, in each case, they were adequately sampled by the lidar. Figure 6 shows the results for the four example nights. As with the O<sub>2</sub> reanalysis, excellent agreement was obtained on three of the four nights with nocturnal rms deviation less than 4 K. Only on 9 July did significant differences arise during the first  $\sim 3$  hours of observations (rms 7.2 K), which was somewhat improved over that of the fixed altitude study. Thereafter, near-full agreement between the lidar and the MTM data was achieved. Computed altitudes during the course of these four nights ranged from  $\sim 84$  to 92 km.

[32] At this point, we note that our studies utilized a fixed Gaussian shape for the layer profile and no account of possible changes in the shape and width of the emission layer with time has been made. *Melo et al.* [2001] have shown that unusually high temperatures ( $\sim 270$ K), can significantly alter the height, width and shape of the OH emission profile, due to the inverse dependence of the volume emission rate on temperature. However, our data did not exhibit such temperature extremes and this effect is not thought to be significant for the measurement presented herein.

[33] A summary of the results of this reanalysis for all 16 nights of coincident data is also included in Table 2, alongside the fixed altitude results. In every case, the nightly rms mean difference is significantly improved over the fixed altitude study. This result holds true for both the

O<sub>2</sub> and the OH data comparisons. For the O<sub>2</sub> study, the average rms decreased by a factor of  $\sim 3$  from 6.6 to 2.4 K. A similar improvement factor was determined for the OH comparison study (6.0 down to 2.1 K). The computed peak altitudes derived from this comparison study are also listed in Table 2. For the O<sub>2</sub> comparison, the mean nightly peak altitudes ranged from  $\sim 93$  to 98 km with an average of  $94.6 \pm 0.3$  km. For the OH study, the mean nocturnal peak altitude was  $88.7 \pm 0.5$  km (range  $\sim 86$  to 92 km). Thus, by allowing the altitude of the Gaussian profile to vary over a finite, but physically reasonable height range, we have significantly improved our comparison of these two independent temperature data sets.

[34] Figure 7 plots the distribution of the computed altitudes for both the OH/lidar and O<sub>2</sub>/lidar data sets. These two histograms provide additional information on the height variability determined during the course of the 16 nights of joint data. Furthermore, the shape of the distribution can be used to help quantify the expected altitude variability. This is indicated by the solid curves which show a Gaussian fit to the two data sets. The O<sub>2</sub> data (Figure 7b) indicate a broad distribution over the height range  $\sim 91$ – $98$  km and a Gaussian mean of 94.4 km (standard deviation 4.2 km); in very good agreement with the nominal altitude and range reported in the literature [e.g., *Witt et al.*, 1979; *Watanabe et al.*, 1981; *Murtagh et al.*, 1990]. The OH distribution (Figure 7a) exhibits a clearer preference for peak altitudes in the range of  $\sim 86$ – $92$  km with a mean at 88.6 km (standard deviation 3.0 km). This also agrees very well with prior height measurements [e.g., *Yee et al.*, 1997], but is slightly higher than that suggested by *Baker and Stair* [1988], as a recommended working number of  $86.8 \pm 2.6$  km in their seminal study of rocket soundings. To determine how much improvement this new mean OH altitude would produce, we have further investigated the lidar/OH data set, this time assuming a fixed height of 89 km. The results of this study are also listed in Table 2 (under column ΔT (89)) and show a slight improvement in most, but not all cases,

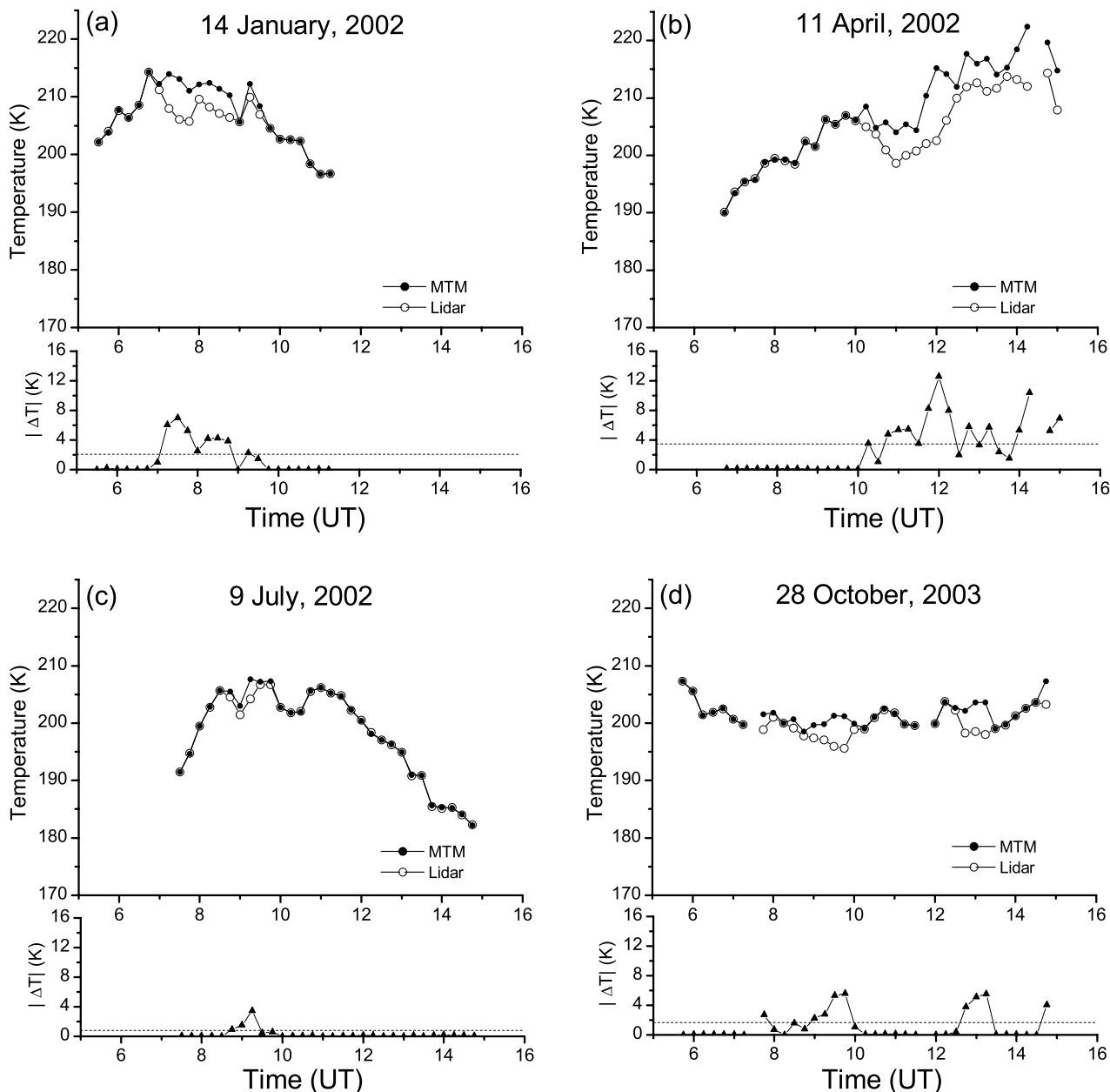


**Figure 5.** Comparison of the Gaussian-weighted lidar temperature data (open circles) with the O<sub>2</sub> MTM (solid circles) data for peak altitudes varying by  $\pm 6$  km. Results for the four example nights are shown together with their rms deviation illustrating significant improvement in the temperature comparison.

resulting in an average nightly rms difference of 4.7 K (compared with 6.0 K for 87 km altitude).

#### 4. Discussion

[35] The high degree of agreement that is evident between the lidar and MTM temperature measurements presented here on a point-to-point as well as on a nightly mean basis, establishes the validity of these two measurement techniques and provides high confidence for further long-term coordinated measurements. Within our measurement uncertainties, this result holds true for assumed altitudes of 87 and 94 km for the OH and O<sub>2</sub> emissions respectively, but as we have also shown, this result can be significantly improved when the altitude of the emission layers is allowed

to vary with time, over a physically reasonable range, and yielding essentially identical nightly mean values.

[36] Previous coordinated lidar and airglow temperature investigations have focused on determining the mean height of the emission layer that is presumed to be constant, and no meaningful attempts have been made to investigate height changes during the course of the night [e.g., *von Zahn et al.*, 1987; *She and Lowe*, 1998]. This said, theoretical studies and limited satellite measurements have shown that systematic changes in the height of the emission layers can occur possibly due to tides and gravity waves [*Ward*, 1998; *Zhang et al.*, 2001]. In particular, *Shepherd et al.* [1995] observed large variations in the OI (557.7 nm) emission at equatorial latitudes, using the WINDII instrument on the UARS satellite, which exhibited a strong local time dependence.

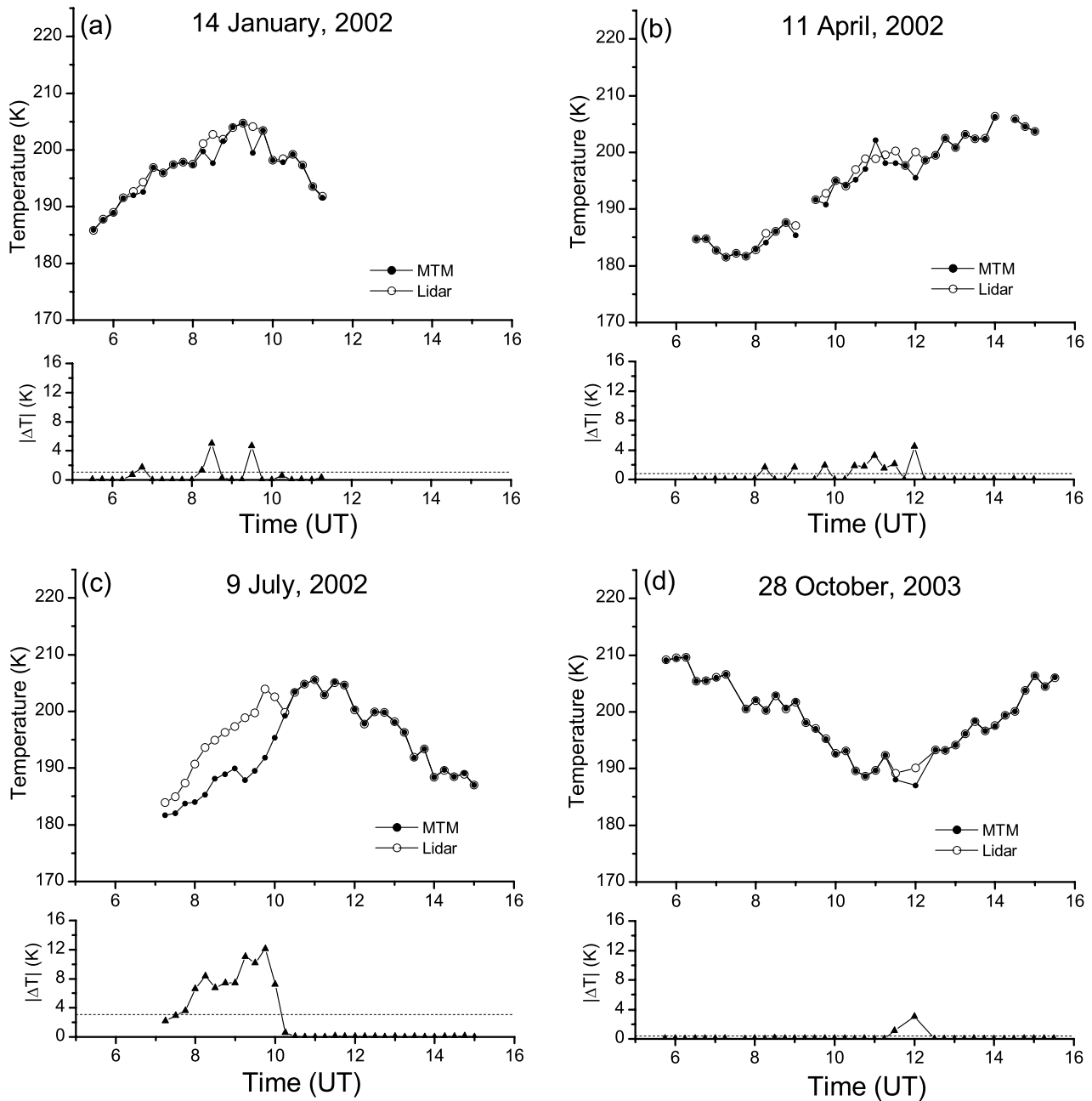


**Figure 6.** Same as Figure 5, but for the OH example data.

Altitude measurements showed an intense airglow layer at dusk that descended from the mean altitude of 95 km down to about 89 km by local midnight. After midnight, a much weaker layer appeared at higher altitudes. The strong local time dependence was suggested to be due to the diurnal tide. Subsequently, *Roble and Shepherd [1997]* utilized TIME-GCM simulations to show that the equatorial diurnal tide has sufficient amplitude to significantly alter the atomic oxygen distribution at low-latitude to produce the observed strong 557.7 nm variation. To investigate the nature and local time variability in altitude inferred from our temperature comparison study, we have further examined the data to look for evidence of tidal (or long-period wave) signatures in the altitude results.

[37] Figure 8a plots the peak altitude as a function of time derived from our lidar/MTM comparison study of 11 April. The upper plot (solid circles) shows the  $O_2$  altitude variation computed from our previous analysis that was used to minimize the differences between the two data sets. The 15-min data samples have been 5-point smoothed to emphasize the general trend in the plot and to minimize point-to-point variability associated with the measurement uncertainties in the two data sets. A significant downward trend in altitude is evident during the course of the night; with the peak altitude occurring initially at  $\sim 96$  km and then reducing monotonically down to  $\sim 90$  km over a period of  $\sim 8$  hours. A pronounced wave-like perturbation is also superimposed on this trend. The dashed line shows a least

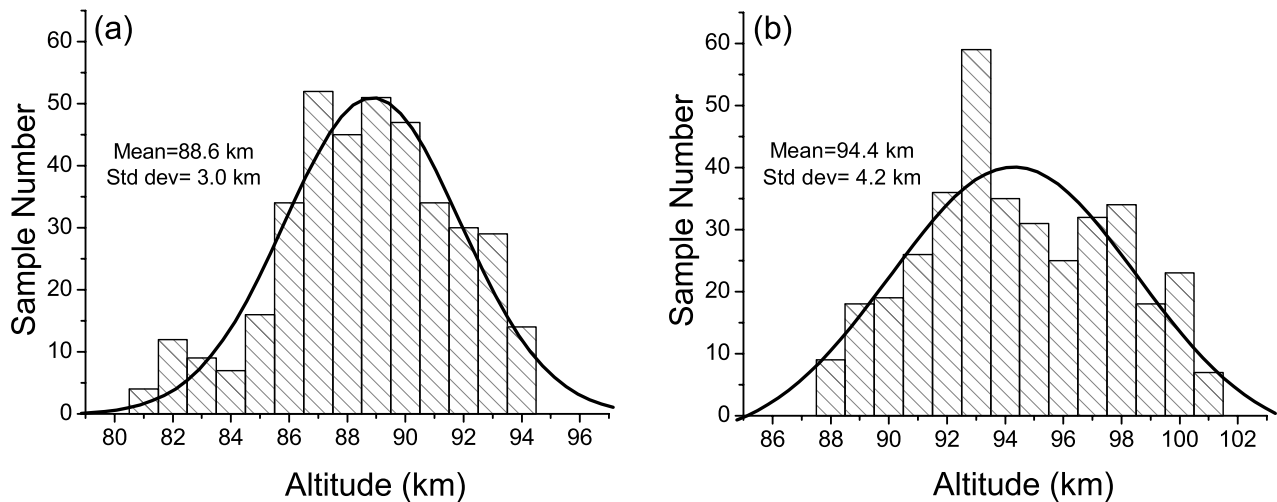


**Figure 7.** Histograms showing the distribution of computed altitudes for (a) OH and (b) O<sub>2</sub> using the 16 nights of coincident lidar and MTM measurements. The solid curves show a Gaussian fit to the two data sets.

squares fit to the inferred change in peak altitude as a function of time and indicates a slope of  $-0.8 \pm 0.1$  km/h.

[38] The lower plot (open circles) indicates the apparent trend determined from the OH/lidar comparison for this night. A similar-magnitude downward trend is also evident with superimposed shorter-period wave structure. The least squares fit is comparable to the O<sub>2</sub> altitudinal data at  $-0.6 \pm 0.07$  km/h. Figure 8b shows the coincident lidar data. The two solid lines superimposed on this contour plot indicate the least squares trends as determined from the OH and O<sub>2</sub> height analysis. As discussed earlier, the lidar data are dominated by a strong diurnal tidal perturbation. It is evident that both trends appear to track the phase of this tidal perturbation quite closely. This suggests that the instantaneous altitudes of both emission layers

were strongly influenced by the downward phase progression of the diurnal tidal perturbation on this occasion.

[39] Independent evidence in support of a significant altitude change in the O<sub>2</sub> nightglow emission is provided by the TIMED Doppler Interferometer (TIDI) instrument on the TIMED satellite, which sampled the upper atmospheric O<sub>2</sub> (0,0) emission over Hawaii at two times during this night. The first measurement was made at 07:28 UT. TIDI measures the limb brightness profile for the O<sub>2</sub> (0, 0) from which the volume emission rate (VER) profile is derived with a vertical resolution of 2.5 km [e.g., Killeen *et al.*, 1999]. This emission is not observable from the ground due to self-absorption by molecular oxygen in the intervening atmosphere; however, it originates from the same airglow source and has the same altitude structure as the O<sub>2</sub> (0,1)

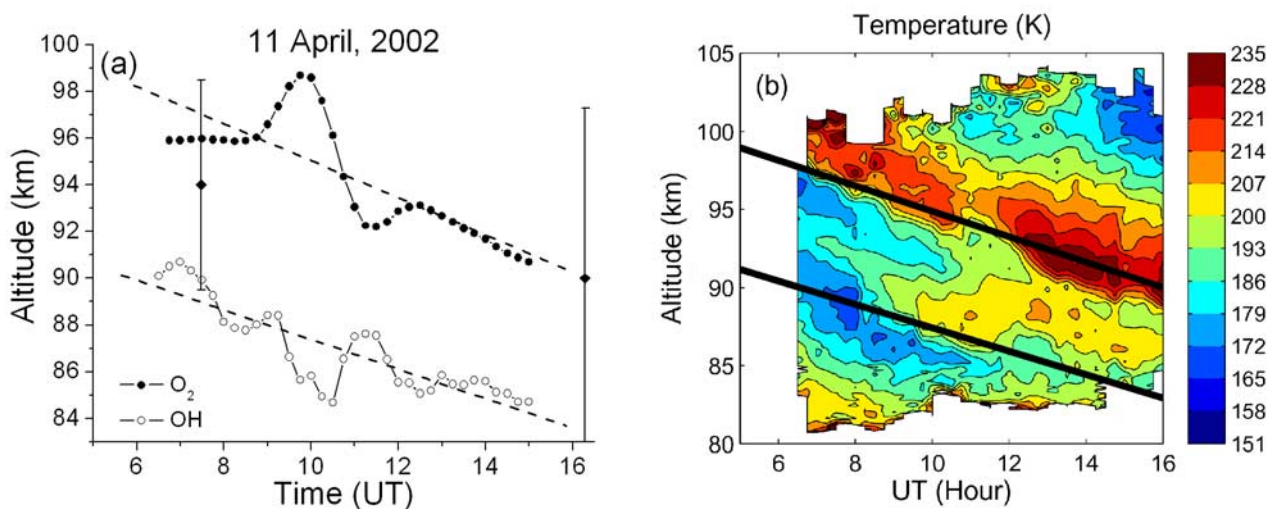


**Figure 8.** (a) Inferred peak altitudes versus time (5-point smoothed) for the O<sub>2</sub> (solid circles) and OH (open circles) data, and (b) coincident lidar temperature contours for 11 April. The dashed lines in Figure 8a indicate the least squares fits to the OH and O<sub>2</sub> peak altitude data and are also shown in Figure 8b as the solid lines apparently tracking the phase of the tidal perturbation. The “I bars” in Figure 8a indicate altitude measurements by the TIDI instrument on the TIMED satellite during two overpasses.

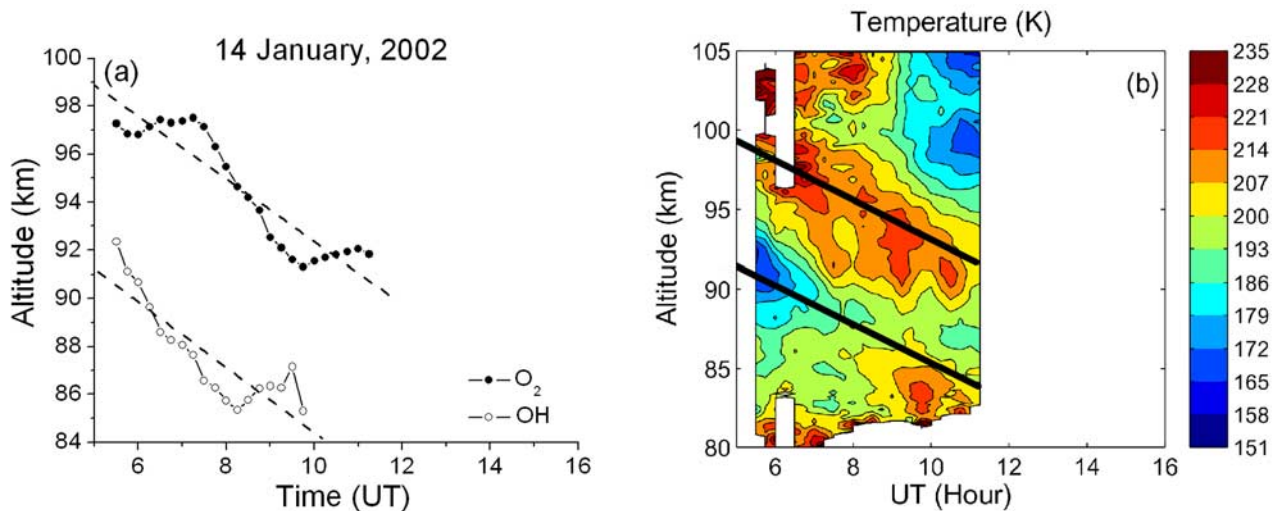


**Figure 9.** Same as Figure 8, but for the 14 January results. Note that there are no coincident TIDI/TIMED data on this occasion.

band emission that is measured by the MTM. A Gaussian fit to the VER profile yielded a peak altitude for the emission layer of  $\sim 94$  km (FWHM = 8.9 km). A second overpass was obtained over 8 hours later at 16:17 UT indicating a lower peak altitude  $\sim 90$  km and a somewhat broader layer width (FWHM = 14.6 km). These results are also indicated on the figure by the “I” bar (the size of which represents the observed thickness of the emission layer). These two measurements were made within  $\sim 300$  km of Maui, but over a much larger geographic sample area, and suggest that the altitude of the emission layer decreased significantly during the night in good agreement with our joint lidar/MTM results.

[40] Figure 9 shows the results of a similar analysis applied to the 14 January data. For comparison, the altitude and temporal scales are the same as those used in Figure 8. On this occasion, the MTM temperature data (Figure 2a) indicated a quasi-12-hour periodicity, possibly associated with a semidiurnal tidal perturbation. These observations were supported by the lidar measurements which showed a steeper downward phase progression, indicative of a significantly larger vertical wavelength ( $\sim 40$ – $50$  km) perturbation. The  $O_2$  and the OH plots of Figure 9 both show a decrease in the altitudes of the emission layers during the  $\sim 5$  hours of coincident measurements. The altitude change for the  $O_2$  layer was 5.5 km and 7.0 km for the OH layer, similar in magnitude to the change evident in Figure 8. The least squares computed slopes were  $-1.3 \pm 0.1$  km/h ( $O_2$ ) and  $-1.4 \pm 0.2$  km/h (OH). These trends are also indicated by the solid lines on the lidar contour plot in Figure 9. As with the previous example, the slopes again line up reasonably well with the downward phase progression evident in the lidar data. (Note: on this occasion, the OH/lidar comparisons are of shorter duration than the  $O_2$ /lidar comparison due to the reduced Na signal levels below  $\sim 85$  km.) Thus, during times when the joint lidar and MTM data sets were dominated by strong tide-like perturbation, our analysis suggests that the altitude of both airglow emissions tend to track the downward phase progression of the perturbations. These results are quite consistent with the  $O_2$  trend

appearing to track the warm phase of the tides in both examples, while the OH data tracked the underlying cold phase of the tidal perturbations.

[41] The above analysis utilized data from two independent measurements of the mesospheric temperature, both of which have associated uncertainties in their absolute magnitudes. If our joint temperature determinations were subject to unexpectedly large uncertainties, then this method of analysis would not be expected to produce the observed systematic variations. Furthermore, we would not expect the OH and  $O_2$  lidar-temperature comparisons to show similar trends as they are determined independently from separate intensity data. However, our height analysis method does compare absolute temperature data from both instruments which are subject to uncertainties of about  $\pm 5$  K (MTM) and  $\pm 1$ – $2$  K (lidar). Although not evident in our comparative temperature analysis, we have investigated the effects of a possible systematic difference in the MTM and lidar temperature data on the peak altitude variation with local time. To do this, we further analyzed the data of Figures 8 and 9 assuming that the observations are subject to a systematic offset of  $\pm 5$  K. Given the quality of the data agreement listed in Table 2, this analysis is expected to encompass any differences in the two data sets and will provide an estimate of the uncertainties in the deduced altitude trends. Figure 10 shows the results of this analysis for 14 January (Figure 10a) and 11 April (Figure 10b) applied to the lidar/MTM  $O_2$  data. As this emission resides near the centroid of the Na lidar measurements, it permits a best possible comparison. (A similar analysis was not practical for the lidar/OH temperature data as the lower ( $-5$  K) limit often fell outside the lower range of the lidar measurements.) In Figure 10, the solid circles reproduced the altitude variations as given in Figures 8 and 9. The dashed lines enclosing this trend show the altitude variation for a systematic increase (decrease) in the MTM temperature of  $\pm 5$  K. These new limits show instantaneous differences of typically  $< 3$  km for the computed altitude as compared with the original results. However, it is evident that the characteristic downward trend remained unaffected in both examples.

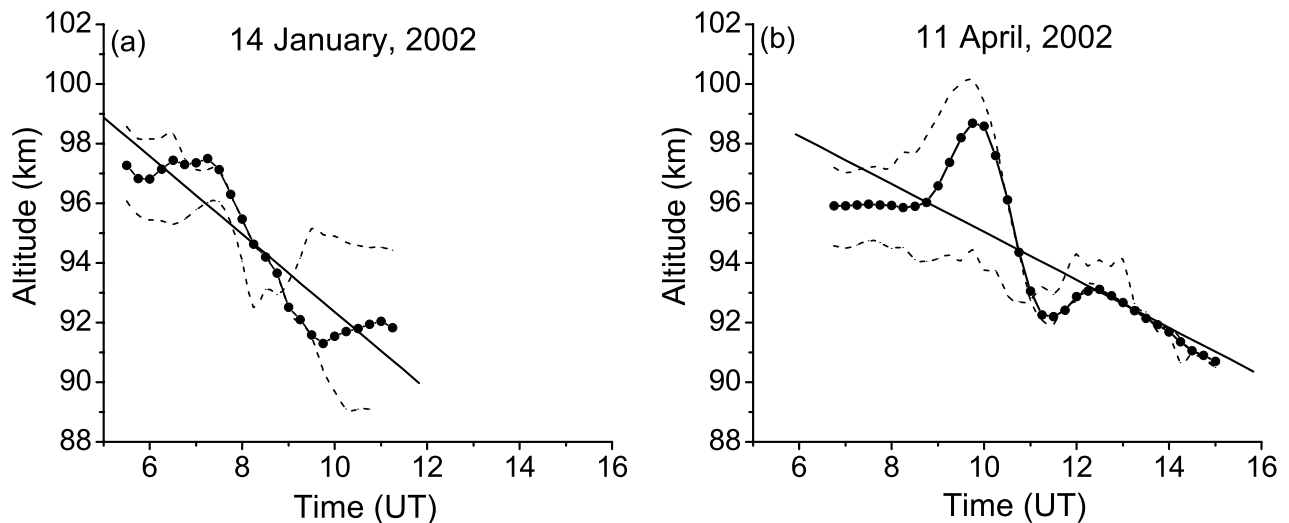


**Figure 10.** Results of  $\pm 5$  K offset applied to the  $O_2$  MTM temperature to help assess the effects of uncertainties in the absolute temperature comparisons. (a) Resultant deviations (dashed lines) from the inferred trend (solid circles). (b) Results for 11 April. In each case the straight lines indicate the least squares fits to the original results of Figures 8 and 9.

This is emphasized by the solid lines which show the fit to the original data, in each case. Thus we conclude that the observed trends in altitude were not significantly affected by any uncertainties in our absolute temperature measurements and the results therefore seem quite reasonable.

[42] Figure 11 shows a compendium of 7 of the 16 nights of data illustrating the consistency in the inferred downward trend in altitude and in time. They include sample nights from each of the seasons that were clearly characterized by large tide-like perturbations, including strong diurnal, semi-diurnal and possibly terdiurnal tidal components. Organized altitude changes evident during the course of the night varied from  $\sim 2$ –7 km. On other occasions, when the forcing was significantly reduced or complex in nature, no systematic trends were detected. These (limited) results indicate a significant altitude change of several km is a normal occurrence in association with strong tidal activity as observed over Maui.

[43] Of key importance to this finding are the UARS satellite and TIME-GCM modeling studies by *Roble and Shepherd* [1997] which showed that only when large diurnal tidal forcing was used in the model did it produce the observed downward motion of the  $OI(557.7 \text{ nm})$  airglow layer. (Weaker tides were not able to penetrate up into the oxygen-rich layer due to gravity wave damping at lower altitudes.) Previous measurements during the fall period at Maui ( $21^\circ\text{N}$ ) have also indicated the presences of much larger than expected diurnal and semi-diurnal tidal amplitudes. In particular, *Dao et al.* [1995] utilized combined Rayleigh and Na lidar observations at Maui to investigate the amplitude of the diurnal tide during the ALOHA-93 campaign (September–October 1993). They reported an exceptionally large tidal amplitude of  $\sim 24$  K (at 90 km) with a vertical wavelength of 25 km (the latter of which is consistent with that expected of the migrating diurnal tide). However, the amplitude was almost 5 times larger than expected from current models at this latitude [e.g., *Hagan et al.*, 1999]. As part of the same campaign, *Hecht et al.*

[1995] reported a large amplitude,  $\sim 19$  K perturbation observed in the  $O_2(0,1)$  band emission that they associated with the semi-diurnal tide. A similar amplitude perturbation was also determined for a concurrent diurnal tidal component, but this latter measurement is subject to some significant uncertainty considering the limited duration of the available data. Subsequently, *Hecht et al.* [1998] included zonally averaged HRDI/UARS daytime temperature observation to compare the measured tidal amplitudes with TIME-GCM model predictions. They concluded that the model significantly underpredicted the diurnal (and possibly the semi-diurnal) temperature perturbations and suggested the possibility of nonmigrating tides as the source of

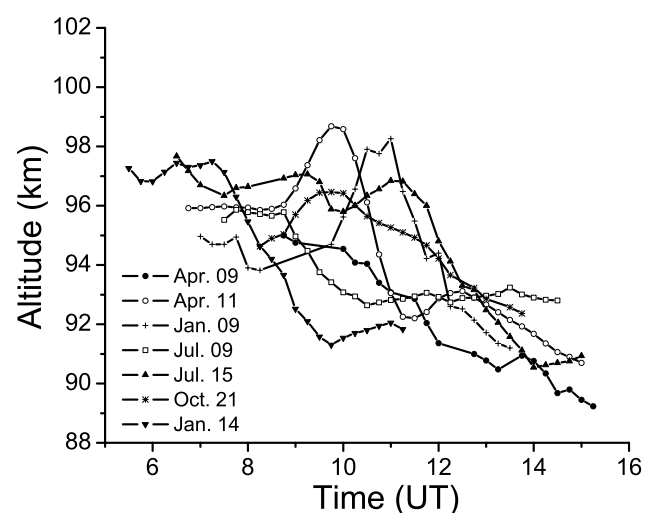


**Figure 11.** Compendium plot of the inferred peak altitude changes with time for 7 of the 16 data nights showing evidence of a consistent downward trend in altitude. On each of these nights the lidar data indicated clear tidal (or long-period gravity wave) activity.

the wave perturbations that they observed (which is not included in the TIME-GCM model).

[44] Our measurements of the slope of the altitudinal trends shown in Figure 11 suggest that they are well-correlated with the tidal phase speeds in each case, but the apparent magnitude of the slopes are slightly smaller. For example, the slope of the altitudinal data for 11 April was  $-0.8 \pm 0.1$  km/h ( $O_2$ ) and  $-0.6 \pm 0.1$  km/h (OH), whereas the diurnal tidal phase speed derived directly from the lidar was  $\sim 1$  km/h. Furthermore, on several occasions no clear trend was observed. The data of 28 October 2003 are intriguing in this regard as they clearly show a well-defined long-period wave ( $\sim 10$  hours) with a downward phase speed of  $\sim 1$  km/h (Figure 3d), but our analysis shows no associated altitude trend. This may be the result of the short vertical wavelength  $\sim 10$  km of this wave, which is similar to the thickness of the airglow emission layers and the perturbation may not have been well resolved in the nightglow data on this occasion. Thus vertical wavelength as well as strong tidal amplitudes are important factors for determining the “visibility” of the altitude trends.

[45] Finally, in addition to the systematic downward trend in altitude evident in Figure 11, significant shorter-period perturbations, possibly associated with concurrent gravity wave activity, are evident in several of the plots. Most recently, *Fujii et al.* [2004] compared simultaneous wind measurements using the MU radar and Fabry-Perot interferometer data to infer altitude changes in the OI (557.7 nm) emission (similar in principle to the technique we have employed herein). Their results were most consistent with a periodic height change of  $\sim 1.5$  km associated with an  $\sim 5.7$ -hour periodicity gravity wave that was also evident in the wind data. This new result shows that long-period gravity waves can also modulate the altitude of the airglow layers. As gravity waves are not the focus of this paper, we intend to investigate their signatures in a separate study.

## 5. Summary

[46] The high quality of the lidar and nightglow temperature data presented herein reflects the current capabilities of improved instrumentation for novel collaborative investigations of the MLT dynamics. A key aspect of the coordinated optical and radar cluster measurements that are performed by the Maui-MALT research program is the ability to utilize multiple data sets for in-depth analyses and modeling studies. The lidar and MTM data are highly complementary in this regard as they provide detailed height-resolved data during limited campaign periods that are linked together by long-term OH and  $O_2$  nightglow temperature measurements at two nominal altitudes within the MLT region. In particular, this comparison study firmly establishes a high-degree of compatibility between these two independent temperature data sets on a nocturnal mean basis (similar to previous analyses in the literature), but also on a point-to-point (15-min resolution) basis providing excellent confidence for further detailed long-term studies of a large-range of temporal scales encompassing nocturnal, seasonal and inter-annual variability. Two key findings of this study are as follows:

[47] 1. The deduced mean nocturnal altitudes for the OH (6,2) and  $O_2$  (0,1) Atmospheric band emissions were 88.6 km

and 94.4 km, respectively, in very good agreement with previous measurements in the literature for an ensemble of rocket, satellite, and ground-based measurements performed over the past 30 years. The layer altitudes were found to vary  $\pm 3.0$  km for the OH, and  $\pm 4.2$  km for the  $O_2$  data.

[48] 2. For well-defined, strong tidal perturbations, a systematic reduction in the altitude of both nightglow emission layers was inferred that closely tracked the observed downward phase progression of the dominant tidal component. Altitude changes ranged from typically 2–7 km.

[49] This latter result is tentative, but quite reasonable based on the growing, yet still very sparse, information available in the literature concerning the effects of tides on the nightglow layers. In particular, our results show a clear-local time behavior that has not been previously reported. Tides are a ubiquitous feature of the MLT region and can exhibit complex time-varying structures especially when interacting with other planetary wave (and possibly gravity wave) structures. Our results to date suggest that the altitude of the nightglow emission layers would therefore be expected to vary by as much as several km on a nocturnal basis at low-latitudes. Previous investigations showing that the nightglow emissions are most consistent at nominal fixed altitude (as discussed earlier herein) are clearly only an averaged result upon which significant variability in height can and does occur. Further investigations will be performed at Maui, as more joint lidar and MTM data are acquired, to determine the frequency of occurrence of strong tidal forcing and to study the effects of the different tidal components on the nightglow layer heights. We also plan to extend this study to include existing Na lidar and MTM temperature data obtained at the Starfire Optical Range, NM ( $35^\circ N$ ), to investigate height variability and its relationship to prevailing tides at midlatitude.

[50] **Acknowledgments.** We are most grateful P. Kervin, Director of the Maui AEOS Facility, for his continued support of the Maui-MALT program. We kindly acknowledge the Boeing staff and, in particular, we wish to thank R. Taft and S. Ah You for their considerable help with our program logistics and measurements. We thank Qian Wu for the TIDI/TIMED analysis, A. Z. Liu for his assistance with the lidar data processing, W. R. Pendleton Jr., and P. D. Pautet for their very helpful discussions. This research was conducted as part of the Maui-MALT program which is a joint endeavor between the Air Force Office of Scientific Research (AFOSR) and the National Science Foundation (NSF). Financial support for the lidar and MTM observations and data analysis was provided by NSF grants ATM-0003198, ATM-03-38425, and ATM-0003218. As part of this research, Y. Zhao was supported as a Post Doctoral Fellow under NSF grant ATM-0228914 and by an NPOSE subcontract with the Space Dynamics Laboratory, Utah State University (Principle Investigator G. Bingham).

## References

- Baker, D. J., and A. T. Stair Jr. (1988), Rocket experiments of the altitude distributions of the hydroxyl airglow, *Phys. Scr.*, **37**, 611–622.
- Bittner, M., D. Offermann, H.-H. Graef, M. Donner, and K. Hamilton (2002), An 18-year time series of OH rotational temperatures and middle atmosphere decadal variations, *J. Atmos. Sol. Terr. Phys.*, **64**, 1147–1166.
- Burns, G. B., J. R. French, P. A. Greet, F. A. Phillips, P. F. B. Williams, K. Finlayson, and G. Klich (2002), Seasonal variations and inter-year trends in seven years of hydroxyl airglow rotational temperature at Davis station ( $69^\circ S$ ,  $78^\circ E$ ), Antarctica, *J. Atmos. Sol. Terr. Phys.*, **64**, 1167–1174.
- Burrage, M. D., N. Arvin, W. R. Skinner, and P. B. Hays (1994), Observations of the  $O_2$  Atmospheric band nightglow by the High Resolution Doppler Imager, *J. Geophys. Res.*, **99**, 15,017–15,023.
- Burrage, M. D., M. E. Hagan, W. R. Skinner, D. L. Wu, and P. B. Hays (1995), Long-term variability in the solar diurnal tide observed by HRDI and simulated by GSWM, *Geophys. Res. Lett.*, **22**, 2641–2644.
- Chapman, S., and R. S. Lindzen (1970), *Atmospheric Tides*, Springer, New York.

- Chu, X., C. S. Gardner, and G. Papen (2001), Lidar observations of polar mesospheric clouds at South Pole: Diurnal variations, *Geophys. Res. Lett.*, **28**, 1937–1940.
- Chu, X., C. S. Gardner, and S. J. Franke (2005), Nocturnal thermal structure of the MLT region at Maui, Hawaii (20.7°N) and Starfire Optical Range, New Mexico (35°N), *J. Geophys. Res.*, **110**, D09S03, doi:10.1029/2004JD004891.
- Dao, P. D., R. Farley, X. Tao, and C. S. Gardner (1995), Lidar observations of the temperature profile between 25 and 103 km: Evidence of strong tidal perturbation, *Geophys. Res. Lett.*, **22**, 2825–2828.
- Dodd, J. A., S. L. Lipson, J. R. Lowell, P. S. Armstrong, W. A. M. Blumberg, R. M. Nadile, S. M. Adler-Golden, W. J. Marinelli, K. W. Holtzclaw, and B. D. Green (1994), Analysis of hydroxyl earthlimb airglow emissions: Kinetic model for state-to-state dynamics of OH ( $v, N$ ), *J. Geophys. Res.*, **99**, 3559–3585.
- Ejiri, M. K., K. Shiokawa, T. Ogawa, M. Kubota, T. Nakamura, and T. Tsuda (2003), Statistical study of short-period gravity waves in OH and OI nightglow images at two separated sites, *J. Geophys. Res.*, **108**(D21), 4679, doi:10.1029/2002JD002795.
- Forbes, J. M. (1995), Tidal and planetary waves, in *The Upper Mesosphere and Lower Thermosphere: A Review of Experiment and Theory*, *Geophys. Monogr. Ser.*, vol. 87, edited by R. M. Johnson and T. L. Killeen, pp. 67–87, AGU, Washington, D. C.
- Franke, S. J., and D. Thorsen (1993), Mean winds and tides in the upper middle atmosphere at Urbana (40°N, 88°W) during 1991–1992, *J. Geophys. Res.*, **98**, 18,607–18,615.
- Fujii, J., T. Nakamura, T. Tsuda, and K. Shiokawa (2004), Comparison of winds measured by MU radar and Fabry-Perot interferometer and effect of OI5577 airglow height variations, *J. Atmos. Sol. Terr. Phys.*, **66**, 573–583.
- Fukuyama, K. (1976), Airglow variations and dynamics in the lower thermosphere and upper mesosphere-1, Diurnal variation and its seasonal dependency, *J. Atmos. Terr. Phys.*, **38**, 1279–1287.
- Gardner, C. S., X. Tao, and G. C. Papen (1995), Simultaneous lidar observations of vertical wind, temperature, and density profiles in the upper mesosphere: Evidence for nonseparability of atmospheric perturbation spectra, *Geophys. Res. Lett.*, **22**, 2877–2880.
- Goldman, A., W. G. Schoenfeld, D. Goorvitch, C. Chackerian Jr., H. Dothe, F. Melen, M. C. Abrams, and J. E. A. Selby (1998), Updated line parameters for the OH  $X^2\Pi - X^2\Pi(v'', v')$  transitions, *J. Quant. Spectrosc. Radiat. Transfer*, **59**, 453–469.
- Hagan, M. E., and J. M. Forbes (2002), Migrating and nonmigrating diurnal tides in the middle and upper atmosphere excited by tropospheric latent heat release, *J. Geophys. Res.*, **107**(D24), 4754, doi:10.1029/2001JD001236.
- Hagan, M. E., J. M. Forbes, and F. Vial (1995), On modeling migrating solar tides, *Geophys. Res. Lett.*, **22**, 893–896.
- Hagan, M. E., M. D. Burrage, J. M. Forbes, J. Hackney, W. J. Randel, and X. Zhang (1999), GSWM-98: Results for migrating solar tides, *J. Geophys. Res.*, **104**(A4), 6813–6827.
- Hays, P. B., D. L. Wu, M. D. Burrage, D. A. Grell, H. J. Grassl, R. S. Lieberman, A. R. Marshall, Y. T. Morton, D. A. Ortland, and W. R. Skinner (1994), Observations of diurnal tide from space, *J. Atmos. Sci.*, **51**, 3077–3093.
- Hecht, J. H., S. K. Ramsay Howat, R. L. Walterscheid, and J. R. Isler (1995), Observations of variations in airglow emissions during ALOHA-93, *Geophys. Res. Lett.*, **22**, 2817–2820.
- Hecht, J. H., et al. (1998), A comparison of atmospheric tides inferred from observations at the mesopause during ALOHA-93 with the model predictions of the TIME-GCM, *J. Geophys. Res.*, **103**, 6307–6321.
- Hickey, M. P., R. L. Walterscheid, and P. G. Richards (2000), Secular variations of atomic oxygen in the mesopause region induced by transient gravity wave packets, *Geophys. Res. Lett.*, **27**(6), 3599–3602.
- Hocking, W. K., and T. Thayaparan (1997), Simultaneous and collocated observation of winds and tides by MF and meteor radars over London, Canada, *Radio Sci.*, **32**(2), 833–866.
- Isler, J. R., M. J. Taylor, and D. C. Fritts (1997), Observational evidence of wave ducting and evanescence in the mesosphere, *J. Geophys. Res.*, **102**(D22), 26,301–26,313.
- Killeen, T. L., et al. (1999), TIMED Doppler Interferometer (TIDI), *Proc. SPIE*, **3756**, 289–301.
- Liu, A. Z., and G. R. Swenson (2003), A modeling study of O<sub>2</sub> and OH airglow perturbations induced by atmospheric gravity wave, *J. Geophys. Res.*, **108**(D4), 4151, doi:10.1029/2002JD002474.
- Manson, A. H., C. E. Meek, H. Teitelbaum, F. Vial, R. Schindler, D. Kurschner, J. J. Smith, G. J. Fraser, and R. R. Clark (1989), Climatologies of semidiurnal and diurnal tides in the middle atmosphere (70–110 km) at middle latitudes (40–55°), *J. Atmos. Terr. Phys.*, **51**, 579–593.
- Manson, A. H., et al. (2002), Seasonal variations of the semidiurnal and diurnal tides in the MLT: Multi-year MF radar observations from 2–70°N, modeled tides (GSWM, CMAM), *Ann. Geophys.*, **20**, 661–677.
- Melo, S. M. L., R. P. Lowe, W. R. Pendleton Jr., M. J. Taylor, B. Williams, and C. Y. She (2001), Effects of a large mesospheric temperature enhancement on the hydroxyl rotational temperature as observed from the ground, *J. Geophys. Res.*, **106**, 30,381–30,388.
- Meriwether, J. W. (1984), Ground based measurements of mesospheric temperatures by optical means, *MAP Handb.*, **13**, 1–18.
- Meriwether, J. W. (1989), A review of the photochemistry of selected nightglow emission from the mesopause, *J. Geophys. Res.*, **94**, 14,629–14,646.
- Mertens, C. J., M. G. Mlynczak, M. Lopez-Puertas, P. P. Wintersteiner, R. H. Picard, J. R. Winick, L. L. Gordley, and J. M. Russell III (2001), Retrieval of mesospheric and lower thermospheric kinetic temperature from measurements of CO<sub>2</sub> 15- $\mu$ m Earth limb emission under non-LTE conditions, *Geophys. Res. Lett.*, **28**, 1391–1394.
- Murtagh, D. P., G. Witt, J. Stegman, I. C. McDade, E. J. Llewellyn, F. Harris, and R. G. H. Greer (1990), An assessment of proposed O(<sup>1</sup>S) and O<sub>2</sub>(b<sup>1</sup> $\Sigma_g^-$ ) nightglow excitation parameters, *Planet. Space Sci.*, **38**, 43–53.
- Nakamura, T., T. Aoro, T. Tsuda, A. G. Admirato, E. Achmad, and Suranto (2003), Mesospheric gravity waves over a tropical convective region observed by OH airglow imaging in Indonesia, *Geophys. Res. Lett.*, **30**(17), 1882, doi:10.1029/2003GL017619.
- Nielsen, K. P., F. Sigernes, E. Raustein, and C. S. Deehr (2002), The 20-year change of the Svalbard OH-temperatures, *Phys. Chem. Earth*, **27**, 555–561.
- Papen, G. C., W. M. Pfenninger, and D. M. Simonich (1995), Sensitivity analysis of Na narrowband wind-temperature lidar systems, *Appl. Opt.*, **34**, 480–498.
- Pendleton, W. R., Jr., P. J. Espy, and M. R. Hammond (1993), Evidence for nonlocal thermodynamic-equilibrium rotation in the OH nightglow, *J. Geophys. Res.*, **98**, 11,567–11,579.
- Pendleton, W. R., Jr., M. J. Taylor, and L. C. Gardner (2000), Terdiurnal oscillations in OH Meinel rotational temperatures for fall conditions at northern midlatitude sites, *Geophys. Res. Lett.*, **27**(12), 1799–1802.
- Petitdidier, M., and H. Teitelbaum (1977), Lower thermosphere emissions and tides, *Planet. Space Sci.*, **25**, 711–721.
- Plagmann, M. S., H. Marsh, W. J. Baggaley, R. G. T. Bennett, K. A. Deutsch, G. J. Fraser, G. Hernandez, B. N. Lawrence, G. E. Plank, and R. W. Smith (1998), Annual variation of airglow heights derived from wind measurements, *Geophys. Res. Lett.*, **25**(24), 4457–4460.
- Reisin, E. R., and J. Scheer (1996), Characteristics of atmospheric waves in the tidal period range derived from zenith observations of O<sub>2</sub> (0-1) Atmospheric and OH (6-2) airglow at lower midlatitudes, *J. Geophys. Res.*, **101**, 21,223–21,232.
- Roble, R. G., and G. G. Shepherd (1997), An analysis of wind imaging interferometer observations of O(<sup>1</sup>S) equatorial emission rates using the thermosphere-ionosphere mesosphere-electrodynamics general circulation model, *J. Geophys. Res.*, **102**, 2467–2474.
- She, C. Y., and R. P. Lowe (1998), Seasonal temperature variations in the mesopause region at midlatitude: Comparison of lidar and hydroxyl rotational temperatures using WINDII/UARS height profiles, *J. Atmos. Sol. Terr. Phys.*, **60**, 1573–1583.
- She, C. Y., and J. R. Yu (1994), Simultaneous three-frequency Na lidar measurements of radial wind and temperature in the mesopause region, *Geophys. Res. Lett.*, **21**, 1771–1774.
- She, C. Y., S. Chen, B. P. Williams, Z. Hu, D. A. Krueger, and M. E. Hagan (2002), Tides in the mesopause region over Fort Collins, Colorado (41°N, 105°W) based on lidar temperature observations covering full diurnal cycles, *J. Geophys. Res.*, **107**(D18), 4350, doi:10.1029/2001JD001189.
- Shepherd, G. G., C. McLandress, and B. H. Solheim (1995), Tidal influence on O(<sup>1</sup>S) airglow altitudes and emission rates at the geographic equator observed by WINDII, *Geophys. Res. Lett.*, **22**, 275–278.
- Shepherd, G. G., R. G. Roble, S.-P. Zhang, C. McLandress, and R. H. Wiens (1998), Tidal influence on midlatitude airglow: Comparison of satellite and ground-based observations with TIMED-GCM predictions, *J. Geophys. Res.*, **103**, 14,741–14,751.
- Singer, W., J. Bremer, W. K. Hocking, J. Weiss, R. Latteck, and M. Zecha (2003), Temperature and wind tides around the summer mesopause at middle and arctic latitudes, *Adv. Space Res.*, **31**, 2055–2060.
- Sivjee, G. G. (1992), Airglow hydroxyl emissions, *Planet. Space Sci.*, **40**, 235–242.
- Sivjee, G. G., and R. L. Walterscheid (1994), 6-hour zonally symmetrical tidal oscillations of the winter mesopause over the south-pole station, *Planet. Space Sci.*, **42**, 447–453.
- States, R. J., and C. S. Gardner (1998), Influence of the diurnal tide and thermospheric heat sources on the formation of mesospheric temperature inversion layers, *Geophys. Res. Lett.*, **25**, 1483–1486.
- States, R. J., and C. S. Gardner (2000), Thermal structure of the mesopause region (80–105 km) at 40°N latitude, Part I: Seasonal variations, *J. Atmos. Sci.*, **57**, 66–77.

- Swenson, G. R., and C. S. Gardner (1998), Analytical models for the responses of the mesospheric OH and Na layers to atmospheric gravity waves, *J. Geophys. Res.*, *103*(D6), 6271–6294.
- Swenson, G. R., and S. B. Mende (1994), OH-emission and gravity waves (including a breaking wave) in all-sky imagery from Bear Lake, UT, *Geophys. Res. Lett.*, *21*, 2239–2242.
- Swenson, G. R., S. B. Mende, and E. J. Llewellyn (1989), Imaging observations of lower thermospheric O(<sup>1</sup>S) and O<sub>2</sub> airglow emissions from STS9: Implications of height variations, *J. Geophys. Res.*, *94*, 1417–1429.
- Swenson, G. R., M. J. Taylor, P. J. Espy, C. S. Gardner, and X. Tao (1995), ALOHA-93 measurements of intrinsic AGW characteristics using airborne airglow imager and ground-based Na wind/temperature lidar, *Geophys. Res. Lett.*, *22*, 2841–2844.
- Takahashi, H., Y. Sahai, and P. P. Batista (1984), Tidal and solar cycle effects on the OI5577A, NaD and OH (8, 3) airglow emissions observed at 23°S, *Planet. Space Sci.*, *32*, 897–902.
- Takahashi, H., B. R. Clemesha, D. M. Simonich, S. M. L. Melo, N. R. Teixeira, A. Eras, J. Stegman, and G. Witt (1996), Rocket measurements of the equatorial airglow: MULTIFOT 92 database, *J. Atmos. Terr. Phys.*, *58*, 1943–1961.
- Takahashi, H., P. P. Batista, R. A. Buriti, D. Gobbi, T. Nakamura, T. Tsuda, and S. Fukao (1998), Simultaneous measurements of airglow OH emission and meteor wind by a scanning photometer and MU radar, *J. Atmos. Sol. Terr. Phys.*, *60*, 1649–1668.
- Talaat, E. R., and R. S. Lieberman (1999), Nonmigrating diurnal tides in mesospheric and lower-thermospheric winds and temperatures, *J. Atmos. Sci.*, *56*(24), 4073–4087.
- Taori, A., M. J. Taylor, and S. J. Franke (2005), Terdiurnal wave signatures in the upper mesospheric temperature and their association with the wind fields at low latitudes (20°N), *J. Geophys. Res.*, doi:10.1029/2004JD004564, in press.
- Taylor, M. J., and M. J. Hill (1991), Near-infrared imaging of hydroxyl wave structure over an ocean site at low latitudes, *Geophys. Res. Lett.*, *18*, 1333–1336.
- Taylor, M. J., M. B. Bishop, and V. Taylor (1995a), All-sky measurements of short-period waves imaged in the OI (557.7nm), Na (589.2nm), and near-infrared OH and O<sub>2</sub> (0,1) nightglow emissions during the ALOHA-93 campaign, *Geophys. Res. Lett.*, *22*, 2833–2836.
- Taylor, M. J., D. C. Fritts, and J. R. Isler (1995b), Determination of horizontal and vertical structure of an unusual pattern of short-period gravity waves imaged during ALOHA-93, *Geophys. Res. Lett.*, *22*, 2837–2840.
- Taylor, M. J., D. N. Turnbull, and R. P. Lowe (1995c), Spectrometric and imaging measurements of a spectacular gravity wave event observed during the ALOHA-93, *Geophys. Res. Lett.*, *22*, 2849–2852.
- Taylor, M. J., W. R. Pendleton Jr., C. S. Gardner, and R. J. States (1999), Comparison of terdiurnal tidal oscillations in mesospheric OH rotational temperature and Na lidar temperature measurements at midlatitudes for fall/spring conditions, *Earth Planets Space*, *51*, 877–885.
- Taylor, M. J., L. C. Gardner, and W. R. Pendleton Jr. (2001), Long period wave signatures in mesospheric OH Meinel (6,2) band intensity and rotational temperature at midlatitudes, *Adv. Space Res.*, *27*(6–7), 1171–1179.
- Thayaparan, T. (1997), The terdiurnal tide in the mesosphere and lower thermosphere over London, Canada (43°N, 81°W), *J. Geophys. Res.*, *102*, 19,949–19,968.
- von Zahn, U., K. H. Fricke, R. Gerndt, and T. Blix (1987), Mesospheric temperatures and the OH layer height as derived from ground-based lidar and OH\* spectrometry, *J. Atmos. Sol. Terr. Phys.*, *49*, 863–869.
- Walterscheid, R. L., G. G. Sivjee, G. Schubert, and R. M. Hamwey (1986), Large amplitude semidiurnal variations in the polar mesopause: Evidence of a pseudotide, *Nature*, 347–349.
- Walterscheid, R. L., G. Schubert, and D. G. Brinkman (2001), Small-scale gravity waves in the upper mesosphere and lower thermosphere generated by deep tropical convection, *J. Geophys. Res.*, *106*, 31,825–31,832.
- Ward, W. E. (1998), Tidal mechanisms of dynamical influence on oxygen recombination airglow in the mesosphere and lower thermosphere, *Adv. Space Res.*, *21*, 795–805.
- Watanabe, T., M. Nakamura, and T. Ogawa (1981), Rocket measurements of O<sub>2</sub> atmospheric and OH Meinel bands in the airglow, *J. Geophys. Res.*, *86*, 5768–5774.
- Wiens, R. H., S. P. Zhang, R. Peterson, and G. G. Shepherd (1995), Tides in emission rate and temperature from the O<sub>2</sub> nightglow over Bear Lake Observatory, *Geophys. Res. Lett.*, *22*, 2637–2640.
- Witt, G., J. Stegman, B. H. Solheim, and E. J. Llewellyn (1979), A measurement of the O<sub>2</sub> ( $b^1\Sigma_g^+ - X^2\Sigma_g^-$ ) Atmospheric band and the OI (<sup>1</sup>S) green line in the nightglow, *Planet. Space Sci.*, *27*, 341–350.
- Wu, Q., and T. L. Killeen (1996), Seasonal dependence of mesospheric gravity waves (<100 km) at Peach Mountain observatory, Michigan, *Geophys. Res. Lett.*, *23*, 2211–2214.
- Yee, J. H., G. Growley, R. G. Roble, W. R. Skinner, M. D. Burrage, and P. B. Hays (1997), Global simulations and observations of O(<sup>1</sup>S), O<sub>2</sub>(<sup>1</sup>Σ), and OH mesospheric nightglow emissions, *J. Geophys. Res.*, *102*, 19,949–19,968.
- Zhang, S. P., R. G. Roble, and G. G. Shepherd (2001), Tidal influence on the oxygen and hydroxyl nightglows: Wind Imaging Interferometer observations and thermosphere/ionosphere/mesosphere electrodynamic general circulations, *J. Geophys. Res.*, *106*, 21,381–21,393.
- Zhao, Y., A. Z. Liu, and C. S. Gardner (2003), Measurements of atmospheric stability in the mesopause region at Starfire Optical Range, *J. Atmos. Sol. Terr. Phys.*, *65*, 219–232.

X. Chu, Department of Electrical and Computer Engineering, University of Illinois at Urbana-Champaign, Urbana, IL 61082, USA.

M. J. Taylor and Y. Zhao, Center for Atmospheric and Space Sciences, Utah State University, Logan, UT 84322, USA. (yucheng@cc.usu.edu)